A. P. Alexandrov
RESEARCH INSTITUTE
OF TECHNOLOGY
N I T I

Investigation of corium melt interaction with NPP reactor vessel steel (METCOR) Phase 2

Progress report
01/06/04 – 25/12/04

Investigation of the interaction between the suboxidized molten corium (C 70) with reactor vessel steel under neutral atmosphere above the melt ($T^{max}_{surf.steel}$ »1400°C). Test MC8

Project title	Investigation of Corium Melt Interaction with NPP Reactor Vessel Steel (METCOR, Phase 2), №833.2	
Contracting organization	ISTC	
File code	METCOR2/RPMC8-04	
Project location	Alexandrov Research Institute of Technology of the Federal Atomic Energy Agency. Russia, 188540, Sosnovy Bor, Leningrad Region, NITI	
Project manager	Name	V.B. Khabensky
	Signature	
	Date	

Authors

Dr.(Eng.), Prof.	V. B. Khabensky
Dr.(Eng.)	S. V. Bechta
Ph.D.	V. S. Granovsky
	S. A. Vitol
	E. V. Krushinov
Ph.D.	S. Yu. Kotova
Ph.D.	A. A. Sulatsky
Prof., Associate member of the Russian Academy of Sciences	V. V. Gusarov
Dr.(Eng.), Prof.	Yu. B. Petrov
Ph.D.	I. V. Kulagin
Ph.D.	D. B. Lopukh
Ph.D.	A. Yu. Pechenkov
Ph.D.	I. V. Poznyak
Ph.D.	S. A. Smirnov
	V. I. Almjashev
	V. G. Bliznyuk
	V. R. Bulygin
	E. M. Belyaeva
	E. K. Kalyago
	N. E. Kamensky
	R. A. Kosarevsky
	A. V. Lysenko
	A. P. Martynov
	V. V. Martynov
	E. V. Shevchenko
	A. A. Chertkov

ABSTRACT

The report presents the description and basic results of MC8 test of the ISTC METCOR Phase 2 Project carried out in the NITI, Sosnovy Bor, on the “Rasplav-3” test facility.

The vessel steel ablation rate has been examined in the oxygen-free (argon) atmosphere during the interaction between the former and molten corium C~32, the maximum temperature of the steel specimen surface being ~1400°C.

CONTENTS

Introduction

MC6 and MC8 tests were devoted to investigating the interaction between suboxidized molten corium C-30 with vessel steel specimens at different temperatures of the steel specimen surface. A noticeable steel ablation has been recorded. The depth of ablation corresponds to the position of the isothermal surface in a steel specimen at a temperature value which correlates with the eutectic temperature of the system that forms in the molten corium – steel interaction zone. On the other hand, vessel steel ablation was insignificant in MC5 test with molten corium C-100. Therefore, in accordance with the Work Plan [1] and Experimental Matrix for the METCOR Phase 2 Project, MC8 test with the molten corium C~70 has been carried out in order to check the influence of the degree of corium oxidation on the kinetics and depth of vessel steel ablation.

Test objective

The test was aimed at investigating in the oxygen-free atmosphere (argon) the corrosion rate of vessel steel at its interaction with molten corium C~70 through the crust at the maximum ~1400ºC of the steel specimen surface.

1. Test description

1.1. Test facility layout

The test employed the same crucible as was used in tests MC5, MC6 and MC7. The furnace schematics is given in Fig. 1.1.1, where Z_c и Z_e are coordinates of the specimen and the cooled electromagnetic screen upper tops position relative to the inductor bottom.

Vessel steel specimen (11) used in the test is presented in Fig.1.1.2. In order to evaluate heat fluxes from melt to the specimen and for cooling the zone of coupling the ultrasonic sensor with the specimen, two calorimeters, the top (12) and the bottom (13) ones were provided.

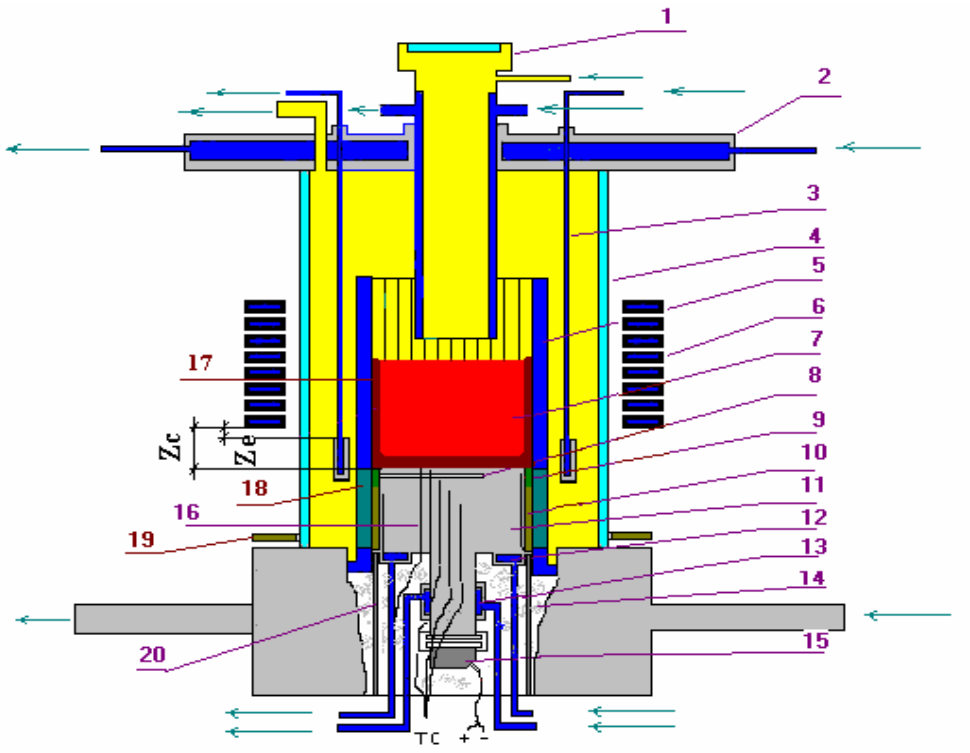

Fig. 1.1.1. Furnace schematics

1 – water-cooled pyrometer shaft; 2 – water-cooled cover; 3 – water-cooled electromagnetic screen; 4 – quartz tube; 5 – crucible section; 6 – inductor; 7 – melt; 8 – acoustic defect; 9 –molten ZrO2 (fianite); 10 –ZrO2 powder; 11 – vessel steel specimen; 12 – top specimen calorimeter; 13 – bottom specimen calorimeter; 14 – mullite wool heat insulation; 15 –ultrasonic sensor; 16 – K-type thermocouples; 17 – crust; 18 – electromagnetic screen (crucible sections are welded); 19 – uncooled electromagnetic screen; 20 – cylindrical support of the specimen.

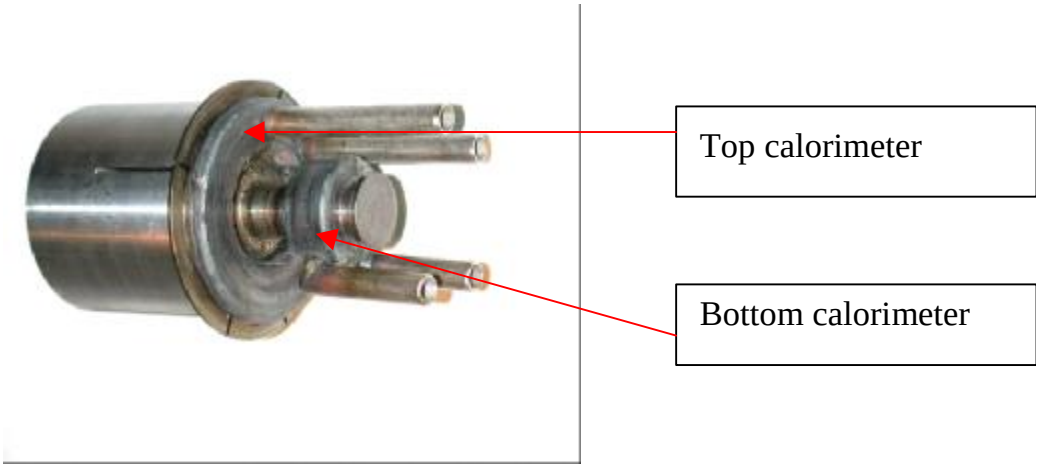

Fig. 1.1.2. Vessel steel specimen

Table 1.1 gives the locations of K-type thermocouple junctions in the specimen. Within a 10 mm radius from the specimen axis the thermocouples were embedded into 1.5 mm-diameter

channels, and within a 29 mm radius – into the 1.5 mm-wide carved grooves.

Table 1.1.1

Thermocouple hot junction locations

Thermocouple No.	α^o (horizontal angle)	r, mm (distance from the specimen axis)	h, mm (distance from the melt-facing top)
TC01	0	10	0
TC02	90	10	2
TC03	45	10	3.5
TC04	135	10	6
TC05	270	10	6
TC06	180	10	7.7
TC07	225	10	20
TC08s	315	29	0
TC09s	90	29	2
TC10s	45	29	4
TC11s	225	29	20
TC12s	180	29	40
TC13s	45	7.5	104

To exclude electromagnetic heating of the specimen, the lower parts of crucible sections were welded together up to above the melt volume, and this arrangement served as an electromagnetic screen (18). Specimen was positioned in the crucible so that its top was 1 mm lower than the top of the welded sections. The gap between the specimen and crucible sections was filled with ZrO_2 powder (10) and pellets of molten stabilized ZrO_2 (9). An additional screening of specimen from electromagnetic heating and the bottom crust thickness control in the molten pool were performed by using water-cooled movable screen (3). Argon-blasted water-cooled steel shaft (1) was used for the melt surface monitoring.

To use the technique of ultrasonic echolocation for controlling the vessel steel corrosion rates, acoustic defect (8) was made in the specimen and the same ultrasonic converter (15) as the one used in MC5, MC6 and MC7 was employed. Air-tightness of the furnace was ensured by quartz tube (4) and water-cooled cover (2).

To control oxygen partial pressure in the gas removed from the furnace and for making up mass balance for the test, a gas-aerosol sampling system was assembled (Fig. 1.1.3). Oxygen content was measured by electrochemical sensor (12). Large area filters (9), switched in turn, were used for purifying the gas from aerosols. Such gas flow parameters as consumption and pressure were controlled at the points indicated in the diagram by the electromechanical flow meters G1 and G2 of OR-40/S type, G3 rotameter and Motorola Pr01, 02, 03 and 06 pressure gauges. Silica gel column (2) was installed at the gas circuit inlet to the furnace for removing traces of moisture from the gas. Gas was supplied from top via shaft (4), thus enabling pyrometric measurements and video recording by blowing aerosols away.

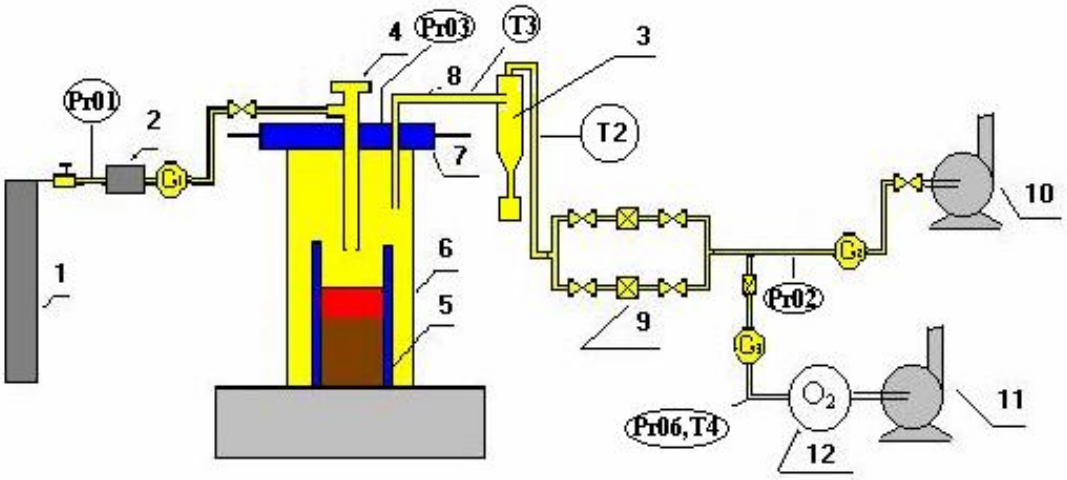

Fig. 1.1.3. Gas in and out

1 – Argon cylinder; 2 – silica gel dehumidifier; 3 – cyclone; 4 – Argon-purged pyrometer shaft; 5 – crucible; 6 – quartz tube; 7 – water-cooled cover; 8 – aerosol pathway; 9 - LAF filters; 10 – fan; 11 – vacuum pump; 12 – oxygen sensor; Pr01-03, Pr06 – pressure gauges; G1, G2– flow meters, G3-rotameter; T2 - T4 – thermocouples.

1.2. Materials

The materials used in the test included 15Kh2NMFA-A vessel steel, urania, zirconia, metallic zirconium, and high-purity argon. All materials have been checked for the main substance content. In addition, the powdered urania was checked by thermogravimetry and the oxygen/uranium ratio was found to equal 2.0. The composition of corium charge is given in Tab. 1.2.1.

Table 1.2.1

Corium charge composition

Component	Main substance content, %	Impurities, %	Notes
UO_2	> 99.0	Fe < 0.03; As < 0.0003; Cu < 0.01; phosphates < 0.002; chlorides < 0.003	Certificate data; thermogravimetry
ZrO_2	(ZrO_2+ HfO_2) > 99.3	Al_2O_3 <0.03; Fe_2O_3 <0.05; CaO <0.03; MgO <0.02; SiO_2 <0.2; TiO_2 <0.1; P_2O_5 <0.15; (Na_2O+K_2O) <0.02	Certificate data
Zr	Нб-1 alloy	Nb <1.0	XRF

The composition and masses of substances loaded into the crucible before melting are given in Tab. 1.2.2.

Table 1.2.2

Composition and masses of substances loaded into the crucible before melting

Purpose	Component	Fraction, μm	Mass, g	Mass, %
Crust	Corium C-66.4 (73.6 mass %UO_2, 19.2 mass % ZrO_2, 7.2 mass % Zr)	< 50	150.0	8.11
Main charge	UO_2	< 100	1259.7	68.09
	ZrO_2	< 100	334.4	18.08
	Metallic Zr	parallelepipeds 15×15×5	105.9	5.72
Total			1850.0	100.00

The required fractions of urania and corium were achieved in argon atmosphere by crushing the pellets from fuel rods and the C-100 corium ingot previously fused in Pr1-MC8 test, respectively. An average sample of the crushed ingot was subjected to XRF and spectrophotometry.
For creating the oxygen-free above-melt atmosphere, high-purity argon was used.

1.3. Experimental procedure

The furnace was blasted with argon for 10 minutes at 10 l/min. It was followed by the startup heating and molten pool production with a crust above its surface (Z_e=10 mm and Z_c=20 mm). The crucible and screen were not moved, and the temperature on the specimen top was stabilized by regulating the valve anode's voltage.

According to thermocouple readings, at 2170 sec the temperature on the specimen top reached approximately 1350ºC, and from that moment (in accordance with the test plan) the vessel steel ablation kinetics at the interaction with corium through the crust was studied during 12 hours in the stabilized temperature regime. Fig.1.3.1. presents the history of heat fluxes into the crucible sections and inductor, of the current applied to the inductor, as well as of the pool surface temperature. It should be noted that in accordance with the test specifications, a crust existed at the molten pool surface throughout the exposure time. The readings of thermocouples in the steel specimen throughout the test are given in Figs.1.3.2 and 1.3.3. Fig 1.3.4 presents the history of heat fluxes into the specimen's top and bottom calorimeters. After the 12-hour exposure, the melt was sampled at 46760 sec and crystallized in argon. The molten pool surface was periodically recorded on video throughout the test.

At 46934 sec heating was disconnected and the ingot with specimen were cooled in argon. The cooled specimen and ingot were extracted to undergo the posttest analyses.

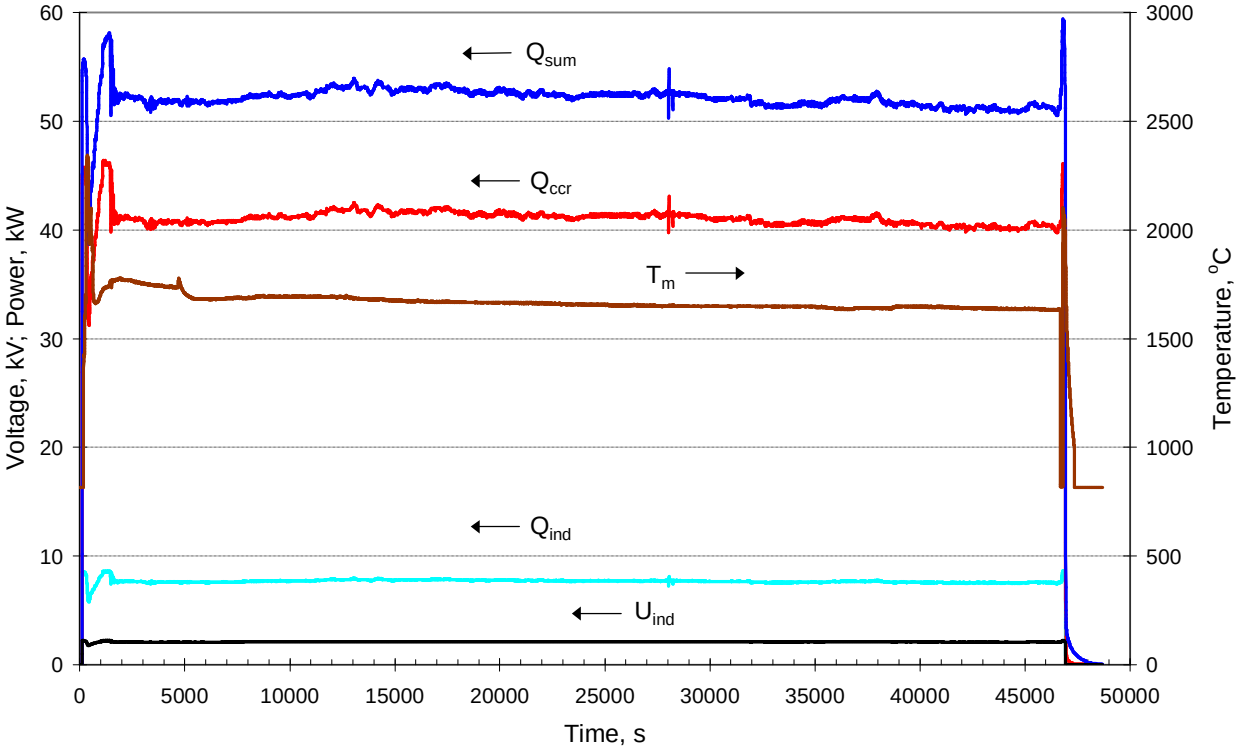

Q_{ccr}- power induced in the crucible; Q_{ind} – power removed from inductor coil by cooling water; Q_{sum} – power to the inductor; T_m-pyrometer readings; U_{ind}- voltage applied to the inductor

Fig. 1.3.1. History of heat and electrical parameters of melting in MC8

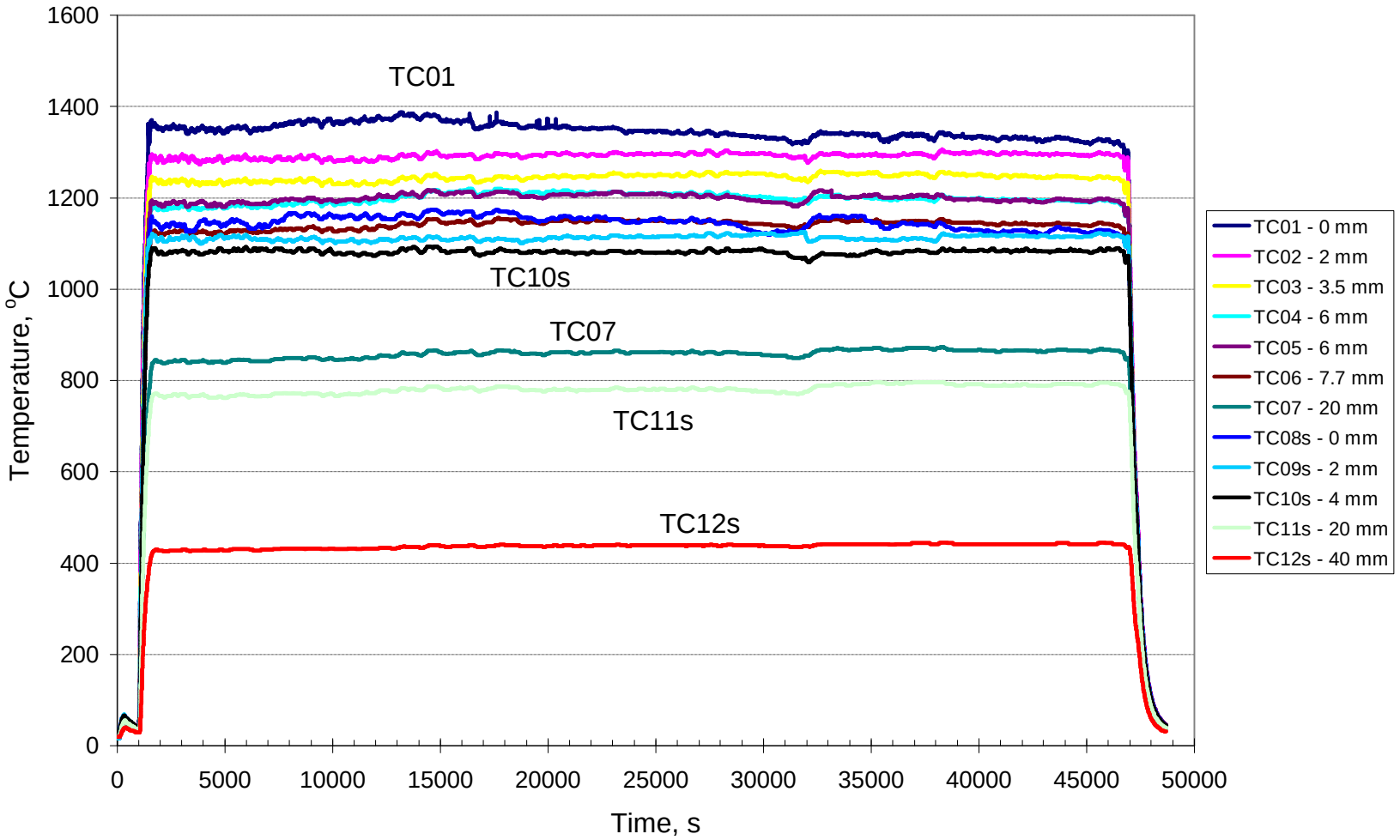

Fig. 1.3.2. Thermocouple readings in MC8

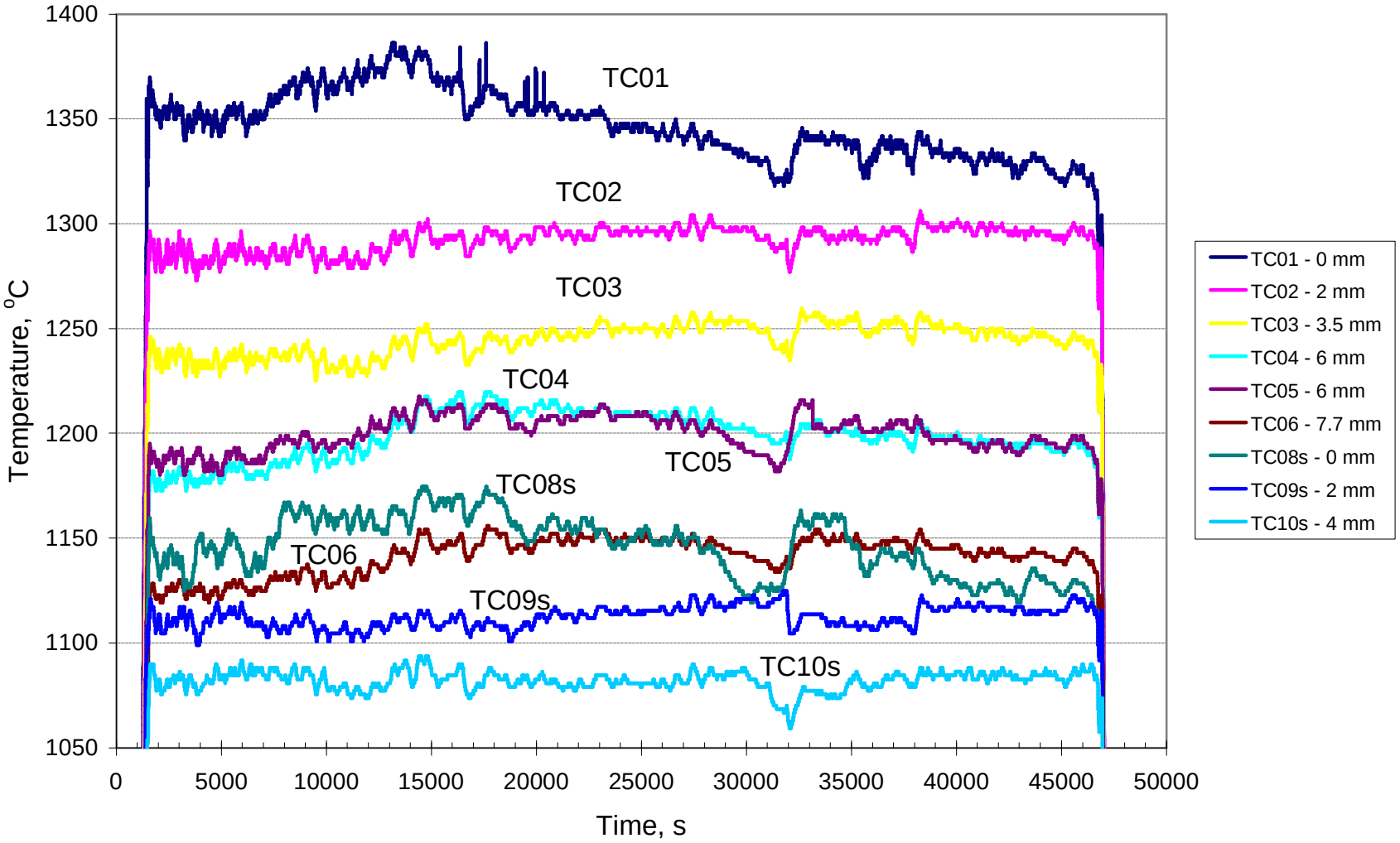

Fig. 1.3.3. Thermocouple readings in MC8

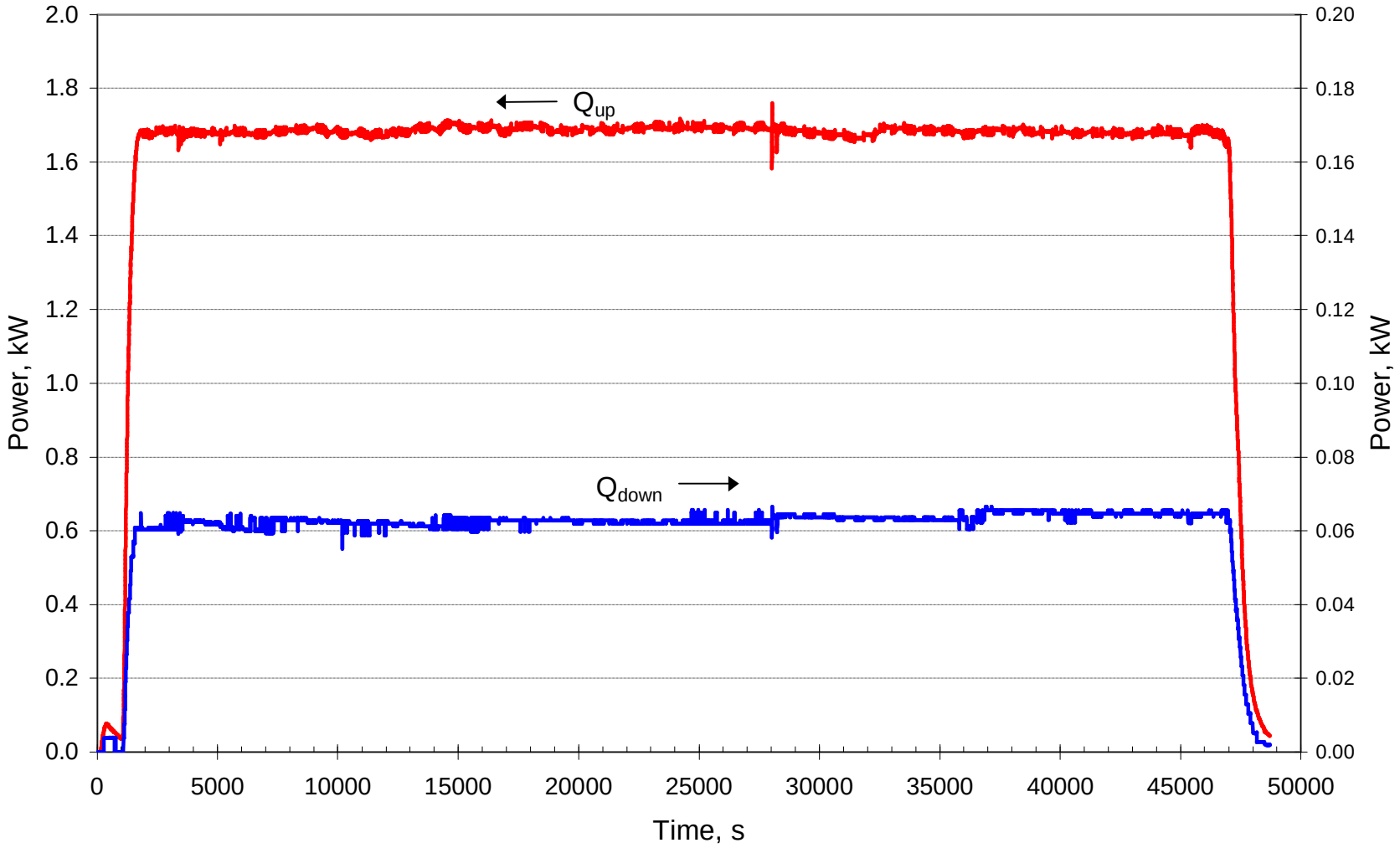

Fig. 1.3.4. History of heat fluxes into the top and bottom calorimeters

2. Posttest analyses

2.1. Numeric modeling of the specimen temperature conditions

In order to determine the temperature and heat flux density at the specimen upper top, calculations of the specimen temperature conditions have been performed in the same way as in the posttest analyses for MC5, 6 and 7. In the calculations a finite-element program was used, which applied the solution of a stationary thermal conductivity equation in the axis-symmetrical formulation. Boundary conditions were fixed as 1) the temperature on the inner surface of the top calorimeter (see Fig. 1.1.1.) estimated at 100°C (calculation results are practically insensitive to the insignificant error of its determination), 2) the temperature on the inner surface of the bottom calorimeter (20°C), and 3) the temperature on the outside surface of peripheral thermal insulation layer (see Fig. 1.1.1.) accepted as equal to the average temperature of cooling water. Thermal conductivity of 15Kh2NMFA-A steel, from which the specimen was produced, was taken from the results of the ISTC METCOR, Phase 1 Project [2]. The heat flux density into the specimen top were varied in the calculations to provide the best agreement between calculated and measured specimen temperatures at the locations of thermocouple junctions. Using the Pr1-MC6 results, the radial distribution of density of the heat flux into the specimen top was determined, as it had been done in MC5.

The results of calculations for the long-term steady-state regime achieved in MC8 are given in Figs. 2.1.1, 2.1.2 and in Tab. 2.1.1. Fig. 2.1.1 a) present the measured and calculated temperatures of the specimen 10 and 29 mm off the specimen axis. Their comparison shows the results of calculations and measurements to be in satisfactory accord. Fig. 2.1.1 b) show the calculated radial temperature distribution across the specimen top. Tab. 2.1.1 gives the calculated heat flux densities to the specimen top (average ones and those in the central ∅15 mm spot), maximum temperatures in the centre of the specimen upper top, as well as the calculated and measured power into the top calorimeter (the power into the bottom calorimeter is negligibly small).

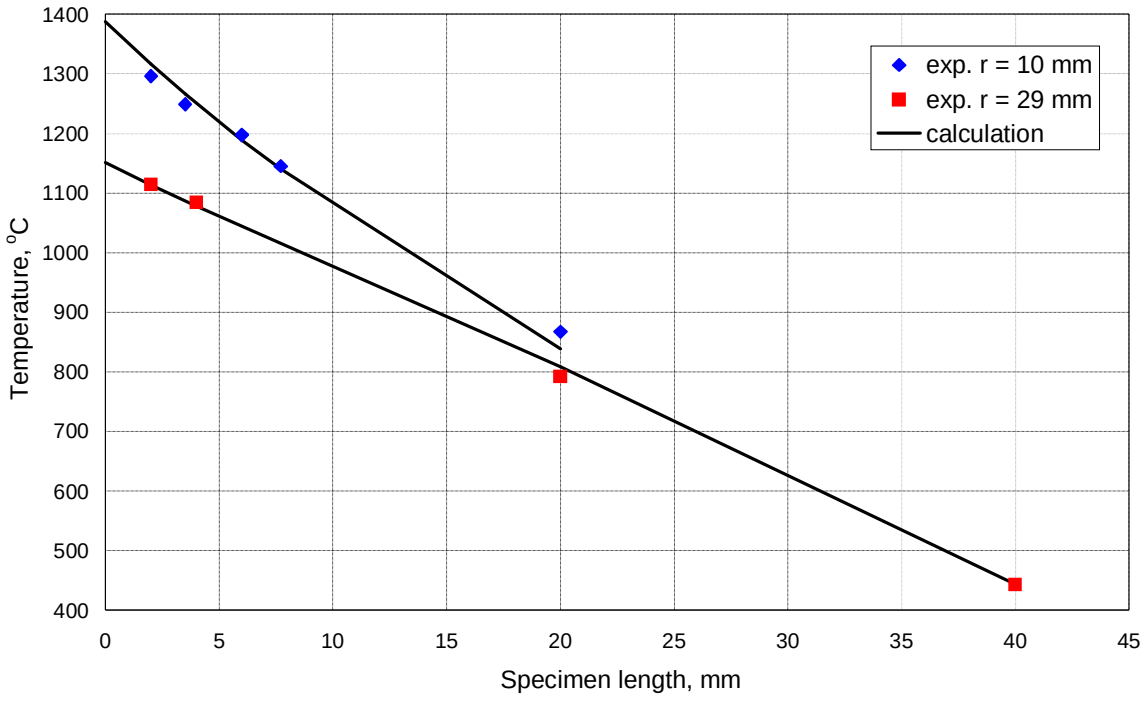

a)

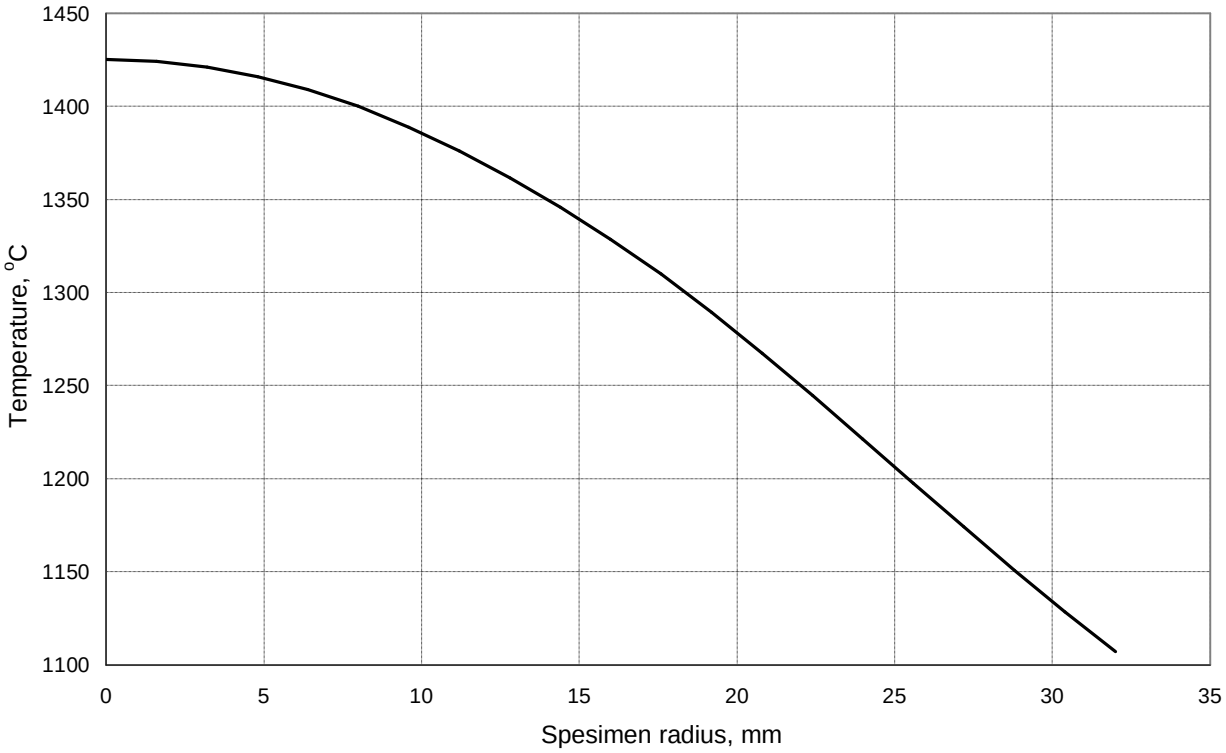

b)

Fig. 2.1.1. Axial (a) and radial (b) distribution of temperatures in the specimen

Table 2.1.1

Calculated and measured power, heat flux and temperature

Heat flux density, average, MW/m^2	Heat flux density, ∅15, MW/m^2	Power into the top calorimeter, calculated, kW	Power into the top calorimeter, measured, kW	Maximum temperature, °C
0,94	1,35	1,85	1,68	1425

Fig. 2.1.2 shows the temperature distribution in the specimen upper part axial section.

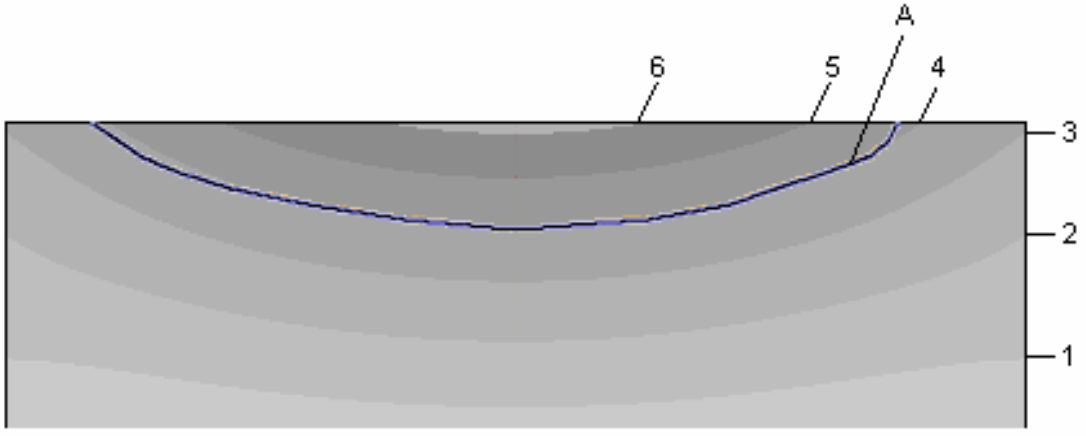

A – interaction zone boundary; 1 - 900°C; 2 – 1000°C; 3 – 1100°C; 4 – 1200°C;

5 – 1300°C; 6 – 1400°C

Fig. 2.1.2. Temperature field in the specimen

Fig. 2.1.2 also shows the interaction zone boundary, the position of which has been determined from the results of posttest measurements. It may be seen that practically along its whole length the said boundary follows the 1200°C isotherm.

2.2. Ultrasonic measurements of the specimen ablation rate

Like in the previous tests, the aim of ultrasonic (US) measurements in MC8 was to determine the kinetics of the corium-steel interaction boundary progress. The methodology for measurements and data processing was explained in detail in the MC5 and MC6 reports. Test MC8 was started with the following values of the main parameters (Tab. 2.2.1).

Table 2.2.1

Initial values of main parameters

Parameter	Notation	Value	Unit	Note
Total specimen length	$L_{tot.}$	102.41	mm	
Distance from the defect to the first point of temperature measurement	l_1	0.037	mm	6.00 mm from the top
Distance from the defect to the second point of temperature measurement	l_2	3.963	mm	2.00 mm from the top
Initial distance from the defect to top	D_0	5.963	mm	
Initial speed of sound in the specimen	C_0	5.94	km/s (mm/μs)	

The value determined in the test for $\beta = \frac{C_0 - C(T)}{TC(T)}$ was $1{,}91 \cdot 10^{-4}$ °C^{-1}.

Fig.2.2.1 shows the array of US signals reflected from the top (D_p) and from the lower boundary of the interaction zone (curve 1) recorded during the test and processed by the subtraction method.

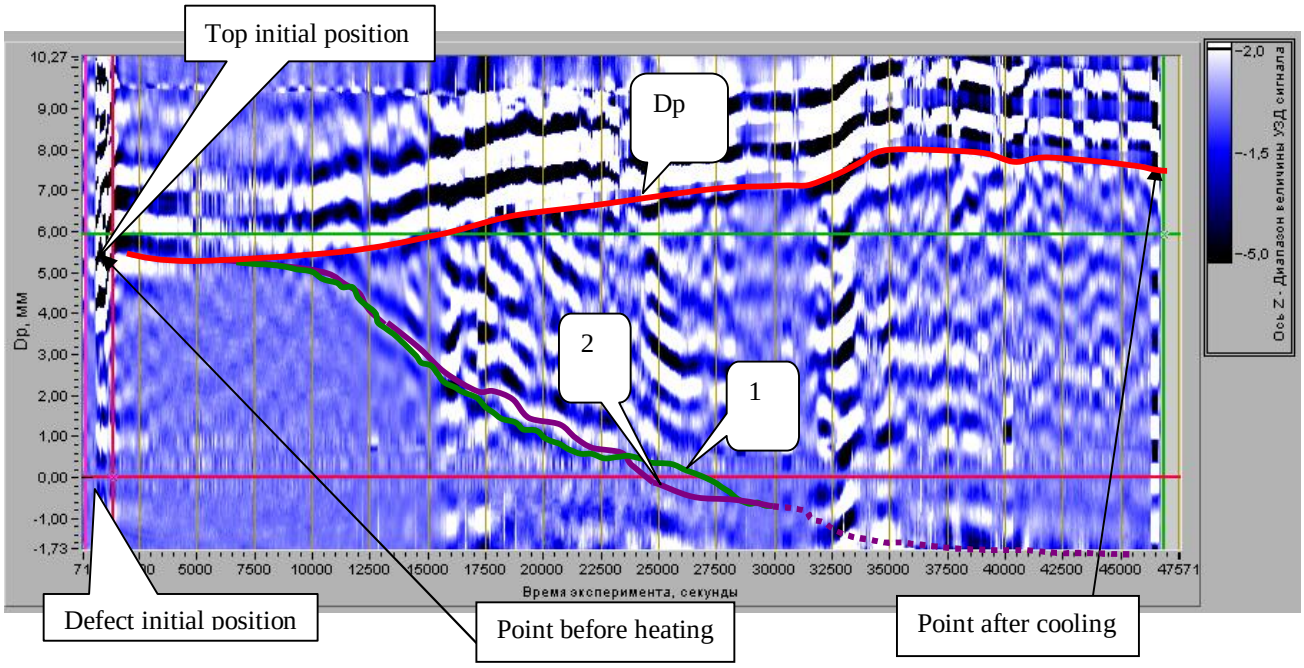

Fig. 2.2.1. US signals array processed by the subtraction method

On the subtraction method

The method of subtraction was applied in MC6, MC7 and MC8 for displaying the changes in the position of the interaction zone lower boundary.

The essence of the subtraction method used to process echograms is: the array $A(t-\Delta t)$ *corresponding to the instant* $t-\Delta t$ *is subtracted from the array* $A(t)$ *corresponding to the instant* t. *If position of the array components has not changed, or changed insignificantly within* Δt, *then the components' amplitudes in the resulting array will be close to zero. If an array component has changed its position considerably, then the resulting component of the array* $A(t)-A(t-\Delta t)$ *will have an amplitude comparable with the initial one. Thus, the resulting array reflects the changed positions of the array components, which correspond to the advance of the interaction zone boundary.*

The above may be illustrated by a simple example. Let us take a monochromatic wave $\sin(x-vt)$ *for a signal and apply the subtraction method to it:*

$$\sin(x-vt)-\sin[x-v(t-\Delta t)]=2\sin v\Delta t\cdot\cos\left(x-vt+\frac{v\Delta t}{2}\right)$$

With the corresponding choice of Dt ($\sin v\Delta t\sim v\Delta t$*) the received signal amplitude is proportionate to the wave propagation speed* v.

As the result of processing by the subtraction method, this signal propagating at a higher speed will have a bigger amplitude and will be easier to identify against the slowly propagating signals.

The Y-line in Fig 2.2.1 shows the true distances between the specimen points and the defect, which are linked with the echogram scanning time by the τ-relation

$$D_p=\frac{0.5C_0(t-t_0)}{1+0.5b(T_s-T_d)},$$

where τ_0 is the time of reference to the signal reflected from the defect, T_s and T_d are the temperatures of the specimen top and of the defect lower point along the specimen axis, respectively.

The analysis of diagrams from Fig. 2.2.1 shows that at the initial stage of interaction between corium and steel specimen minor corrosion of the specimen to a depth of 0.2 mm is observed; the same had been recorded in the previous tests MC6 and MC7. Then, starting from 11000 s, the growth of $D_p(t)$ may be observed, which is due to the formation of the U- and Zr-enriched interaction zone. The speed of sound in the interaction zone is lower than that in the steel specimen, and it leads to the growth of $D_p(t)$ [3]. It should be noted that in MC8 formation of the interaction zone occurred earlier than in MC6 and MC7 (18000 s).

Fig. 2.2.1 shows the advance of the interaction zone lower boundary - $D_p(10000)$-H(t) (curve 1) by the US signals reflected from it. The initial advance rate of 1.17 mm/h gradually decreases to 0.32 mm/h by the time of heating disconnection.

As it is evident from Fig. 2.2.1, by the time of heating disconnection (47000 s), the interaction zone depth measured from the initial position of the specimen top amounted to 7.0 mm. The results of the specimen axial cut posttest examination show the maximum depth of the interaction zone to be 6.7 mm. Therefore, there is a good agreement between the US and posttest measurements.

It should be noted that in the previous tests the advance of the interaction zone lower boundary had to be determined from the $D_p(t)$ data, assuming that H(t) ~ h(t) (H(t) is proportionate to h(t)) [3]. In MC8, the boundary advance data were obtained directly by the US measurements using the US signals reflected from the boundary. Correctness of the assumption that H(t) ~ h(t), postulated when processing the MC6 and MC7 data, was confirmed in the present test by the fact that at t < 31000 s the H(t) ~ h(t) correlation is fulfilled with satisfactory precision (see Fig. 2.2.1, curve 2). At t > 31000 s, perturbance of h(t) was observed, while H(t) stayed smooth. The behaviour of h(t) starting from 31000 s cannot be explained.

The analysis of measurements results in comparison with the previous tests:

1. Like in MC6 and MC7, slow corrosion of the specimen to a dept of 0.2 mm was observed at the initial stage of MC8.
2. The time interval from the temperature regime establishment to the interaction zone formation in MC8 (11000 s) is smaller than in MC6 and MC7 (18000 s).
3. The interaction zone lower boundary in MC8 starts propagating at a rate of 1.17 mm/h and gradually slows down to 0.32 mm/h by the time of heating disconnection.

2.3. Physico-chemical analysis

The performed experimental investigations were aimed at determining:

- qualitative characteristics of vessel steel ablation depending on the oxygen potential of the melt and temperature at the interaction interface;
- microstructure and composition of the transient zone between the steel specimen and corium for developing a model of interaction between molten corium and reactor vessel;
- changes in micro- and macrostructure of the steel specimen after interaction with molten corium.

The above-mentioned tasks solving and correct interpretation of the results obtained required a big volume of posttest analyses. For instance, the samples and templates prepared from the corium ingot and steel specimen (together with the interaction zone), as well as the rod sample taken during the test were subjected to posttest analyses in order to determine the elemental (XRF, chemical analysis) and phase (EDX) compositions, microstructure and properties of materials (optical and scanning electron microscopy, etc.).

2.3.1. Ingot macrostructure

Practically no aerosol deposits were observed on the crucible sections during the furnace disassembly, while above the ingot there was a crust with a mass of 44.1 g (see Fig. 2.3.1.).

During the extraction of the corium ingot and steel specimen from the crucible, the oxidic ingot separated from the steel specimen (Fig. 2.3.2). The oxidic ingot and steel specimen were separately embedded in resin and cut along the axis. Fig. 2.3.2. shows the tops of the corium ingot and steel specimen which have been facing each other during the test. The corium ingot height was 65 mm approximately. The crust between the corium ingot and steel specimen was about 1 mm thick. Fig. 2.3.3 presents longitudinal sections of the corium ingot and steel specimen.

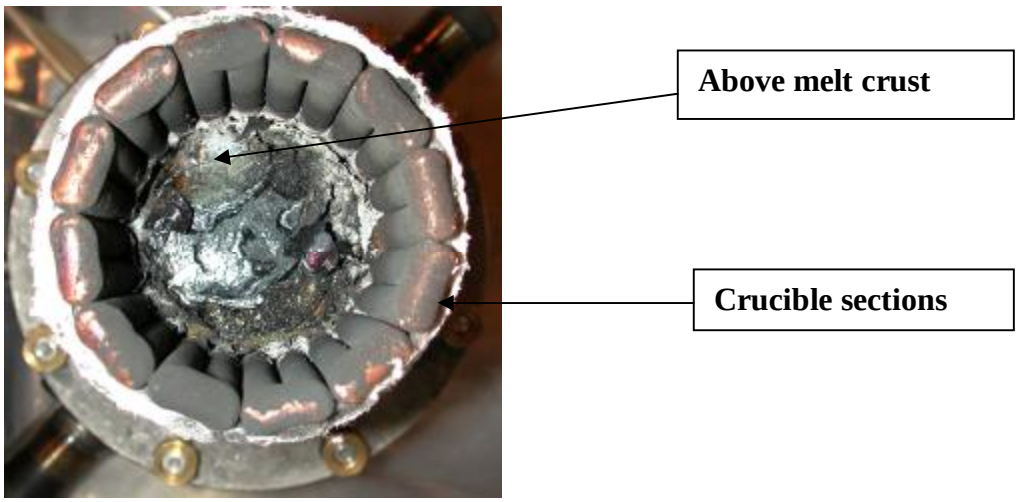

Fig. 2.3.1 Crucible after the test

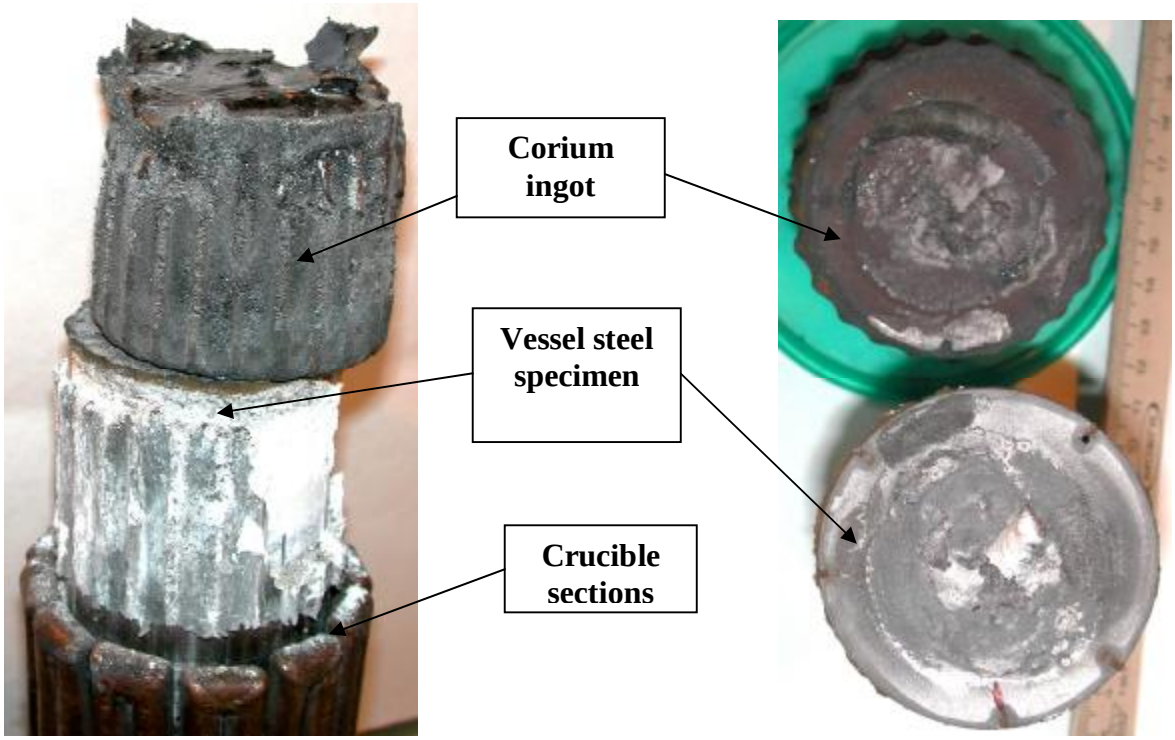

Fig. 2.3.2. Oxidic ingot and steel specimen at their extraction from the crucible, as well as the ingot and specimen tops which have been facing each other during the test

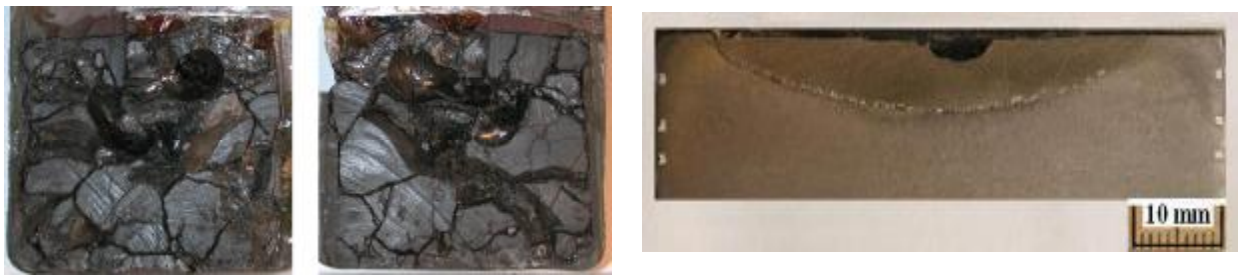

Fig. 2.3.3. Longitudinal sections of the corium ingot and steel specimen

A plate $70 \times 23 \times 8$ mm was cut for SEM/EDX from one half of the ingot from the side of interaction with the steel specimen. The remaining parts of the oxidic ingot were crushed into particles sized below 200 μm and used for taking an average sample by quartering.

2.3.2. Material balance of the test

A separate test Pr1-MC8 was conducted to produce fused corium, 150 g of which were used for imitating actual crust on the steel specimen. The corium ingot produced in Pr1-MC8 was crushed and an average sample was taken by quartering for analytical purposes (see Tab. 2.3.1.).

Table 2.3.1

Results of physico-chemical analysis of the ingot average sample from Pr1-MC8

Determination method	XRF			Volumetric, Zr^0	Zr oxidation degree, C
Element	U	Zr	Impurities and O*		
Ingot average sample, mass %	64.9	21.4	13.7	7.2	66.4

*-from residue.

In order to make the material balance of MC8, the initial charge components and fused products were analyzed for the content of main components and weighed with accuracy up to 0.1 g.

Material balance of components in MC8 is given in Tab. 2.3.2.

Table 2.3.2

MC8 material balance

Introduced into the melt, g		Collected after the test, g	
Corium C-66.2 (73.6 mass %UO_2, 19.5 mass % ZrO_2, 6.8 mass % Zr)	150.0	Rod sample	6.1
UO_2	1259.7	Above melt crust	44.1
ZrO_2	334.4	Ingot	1732.5
Metallic Zr	105.9	Steel specimen	1736.9
Steel specimen	1724.3	Aerosols	3.0
		Spillages*	49.5
Σ	3574.3	Σ	3572.1

*- powders (remaining charge, splashes, etc.).

The debalance is due to the aerosol losses when opening the cover, and to the error of steel specimen weighing.

2.3.3. XRF of the witness specimen and the fused products

The elemental composition of the witness-specimen and the fused products was determined by XRF using the SPARK-1M and SPECTROSCAN MAX-GV spectrometers [4].

Similar to MC5 – MC7, the main components content in the witness steel specimen has been determined by XRF. The XRF results compared with Specifications for the grade of vessel steel in question are given in Tab. 2.3.3.

Table 2.3.3

XRF results for the vessel steel witness specimen. Steel grade 15Kh2NMFA-A

Specs., method of analysis	Chemical elements content, mass %											
	C	Si	Mn	Cr	Ni	Mo	V	P	S	Cu	Co	As
Specs.108-765-78	0.13-0.18	0.17-0.37	0.30-0.60	1.8-2.3	1.0-1.5	0.5-0.7	0.10-0.12	<0.02	<0.02	<0.3	<0.03	<0.003
XRF	-	0.25	0.49	2.24	1.00	0.70	0.10	<0.02	-	0.07	<0.03	<0.003

The XRF data testify to the full compliance of steel used in the tests with Specifications 108-765-78.

The fused products obtained in the test were crushed into particles sized below 200 μm. Then average samples were taken by quartering from the produced powders, ground into particles sized less than 50 μm and analyzed by different methods. All the works were carried out in argon.

Tab. 2.3.4 contains the XRF results for the fused products.

Table 2.3.4

XRF results for the fused products

Sample	Content, mass %			
	U	Zr	Fe	Impurities and O*
Melt rod sample	63.9	20.9	0.02	15.18
Ingot average sample	63.5	20.5	0.3	15.7
Above melt crust	62.1	18.4	2.9	16.6

*O and impurities determined from the residue.

2.3.4. Chemical analysis of the fused products

Both the corium ingot average sample, the rod sample and the above melt crust were checked for the content of U^{+4}, U^{+6}, Fe^{0}, Fe^{2+}, Fe^{3+} and Zr^{0}.

The technique of U+4 and U+6 determination is meant for the determination of uranium microquantities with a sensitivity of 0.04 μg/ml. The technique is based on the formation of stained compounds of the tetravalent uranium and arsenazo III in the 4 N HCl medium. Uranium is reduced by granulated zinc in the presence of ascorbic acid. At the interaction with arsenazo III, the tetravalent uranium yields a complex of green colour, while with the excessive reagent the observed colour is violet of different shades. Spectrophotometry is best with a 2 to 5-time higher molar content of the reagent. Staining occurs almost instantly and is stable for at least two hours. The technique allows determination of the tetravalent uranium and the total uranium in a solution. The quantity of the hexavalent uranium is calculated from the difference between the content of the tetravalent and total uranium [5, 6].

The content of metallic iron, Fe^{0}, was determined in corium by the copper-sulfate method based on the replacement of copper with metallic iron at treating a batch of corium powder with the

copper sulphate solution. Fe^{2+} ions, equivalent to Fe^0, are titrated off with the potassium dichromate solution in the presence of sodium diphenylaminesulphonate, a redox indicator [7,8]. The method allows determination of metallic iron in powdered corium samples with the iron content of less than 0.5%.

The reactions are described by the following equations:

$$Fe + CuSO_4 = FeSO_4 + Cu\downarrow;$$

$$6FeSO_4 + K_2Cr_2O_7 + 7H_2SO_4 = Cr_2(SO_4)_3 + 3Fe_2(SO_4)_3 + K_2SO_4 + 7H_2O.$$

Metallic iron content is calculated by formula:

$$C_{Fe^0} = \frac{(a-b)\cdot T}{H}100\%,$$

a is the quantity of 0.1B potassium dichromate solution used for titration, ml;
b is the quantity of 0.1B potassium dichromate solution used for the solution titration in the control test, ml;
T is the titre of 0.1B potassium dichromate solution expressed in grammes of metallic iron per 1 ml of the solution;
B is the batch that corresponds to the aliquot part of solution taken for titration, g.

The content of ferrous and ferric iron was determined by photocolorimetry with orthophenanthroline. The method is meant for the determination of iron oxides content in samples of the uranium-bearing corium without uranium separation [9]. The range of identified iron concentrations is 0.5-2.0 mg/dm^3. The total relative error of the method does not exceed ±3%, provided the measured optical densities are within 0.2-0.6 range.

The method is based on the reaction of orthophenanthroline (1.10-phenanthroline) with ferrous iron ions, which yields a complex compound with an orange-red colouring. The colour intensity is proportionate to the concentration of iron. Since the bond strength of the complex compound is high (formation constant is $9.8\cdot10^{21}$), optical density does not depend on pH in the 2-9 range. Colouring develops rapidly at pH=3.0-3.5 in presence of excessive orthophenanthroline and keeps stable within several weeks. In more acid solutions the colouring develops slower and is less intense. The direct iron determination is possible at its mass concentration from 0.5 to 2.0 mg/dm^3 [10, 11].

The method allows separate determination of ferrous iron and total iron in a solution. The amount of ferric iron is calculated from the difference between the content of ferrous and total iron [11, 12].

The iron mass concentration is calculated by formula:

$$X = \frac{25C}{V}, \text{ mg/dm}^3,$$

Where C is the iron concentration found from the calibrating diagram, mg/dm^3;
V is the volume of the analyzed aliquot iron sample, cm^3;
25 is the volume to which the sample has been diluted, cm^3.

The final molten corium oxidation degree is calculated from the free zirconium content in the ingot. The volumetric method [13] was used for determining free zirconium in corium. The method is based on measuring the amount of hydrogen, which is liberated at the interaction of metallic zirconium present in corium with concentrated phosphoric acid. The details of free zirconium determination are given in the MC6 report [3].

$$C_n = \frac{Zr_{total} - Zr^0}{Zr_{total}}\cdot 100\%.$$

The results of $Zr_{св.}$, Fe^0, Fe(II), Fe(III), U(IV) and U(VI) determination are summarized in Tab. 2.3.5.

Table 2.3.5

Chemical analysis of corium samples

Detection method	Photocolorimetry				Copper-sulfate, Fe^0	Volumetric, Zr^0
Sample	U^{4+}	U^{6+}	Fe^{2+}	Fe^{3+}		
	mass %					
Above melt crust	61.7	not detected	1.93	not detected	2.08	10.2
Melt rod sample	59.71	not detected	0.23	not detected	0.16	4.98
Ingot average sample	63.22	not detected	0.53	not detected	0.16	8.0

Chemical analysis has shown the absence of U^{6+} and Fe^{3+} in the fused products. Notable is the smaller content of free zirconium in the melt sample if compared to the ingot average sample, which may be due either to the uneven zirconium distribution in the melt under the crust, or to the sample oxidation at taking it from the melt.

Table 2.3.6 gives the errors of the analyses.

Table 2.3.6

Analyses errors

Element	Error, % rel.	Detection method
U^{+6}	5	Photocolorimetry
U^{+4}		
Zr^0	10	Volumetric
Fe^0		Copper-sulfate
Fe^{+2}	5	Photocolorimetry
Fe^{+3}		
U	5	XRF
Zr		
Fe		

A comparison of the XRF and chemical analyses results of the main components in the fused products has shown them to be in satisfactory accord. As a result of the mass transfer and redox processes, some amounts of uranium and zirconium have transferred into the steel specimen from the oxidic part, while steel components have transferred into the oxidic melt in insignificant quantities (see Tabs 2.3.4. and 2.3.5).

The results of corium ingots analyses and the calculated values of the final corium oxidation degrees in MC6-MC8 are compared in Tab. 2.3.7 below. (The ingots produced in MC6 and MC7 had different macrostructure of their upper and lower parts. In order to reveal the differences in their chemical composition, separate average samples have been prepared for analysis from the upper and lower parts of ingots).

Table 2.3.7

Analysis of corium ingots and their final oxidation degrees in MC6-MC8

Test	Actual crust composition				Main charge composition				Corium ingot composition after the test					
	UO_2	ZrO_2	Zr	C	UO_2	ZrO_2	Zr	C	UO_2	ZrO_2	Zr	FeO	Fe	C
	mass %				mass %				mass %					
6	76.4	7.9	15.7	27.0	76.0	9.3	14.7	32.0	72.3[2)]	12.4[2)]	14.7[2)]	0.5[2)]	0.1[2)]	38.5
									70.9[1)]	9.4[1)]	17.8[1)]	1.8[1)]	0.1[1)]	28.0
7	76.4	7.9	15.7	27.0	76.0	9.3	14.7	32.0	73.4[1)]	11.7[1)]	14.2[1)]	0.7[1)]	0.1[1)]	38.0
									75.0[2)]	11.0[2)]	13.5[2)]	0.5[2)]	0.1[2)]	37.7
8	73.6	19.2	7.2	66.4	74.1	19.7	6.2	70.0	67.7	26.8	5.0	0.3	0.2	80.0

[1)]- ingot bottom
[2)]- ingot top

The analyses of the ingot upper and bottom parts from MC6 have shown them to differ greatly as the consequence of maintaining the interaction between corium and steel during the test and of corium crystallization upon test completion. The differences in composition were insignificant (within the analysis error) in MC7, and in MC8 the average sample was prepared from the whole corium ingot which did not have substantial macrostructural differences along its height.

2.3.5. Fused corium density

The bottle density of fused corium was determined from the average sample prepared by quartering [14]. Ethyl alcohol was used as a picnometric liquid. The results of density determination under normal conditions are presented in Tab. 2.3.8.

Table 2.3.8

Fused corium bottle density determination

Sample	Fused corium particle size, μm	Bottle density, g/cm^3
Corium average sample	100-200	8.56

The density evaluation error was ± 0.02 g/cm^3.

The errors of bottle density determination g was below ± 2% for metallic inclusions with a mass from 2 to 10 and ± 5% for those with a mass less than 2 g.

In comparison to MC6 (8.52-8.78 g/cm^3) and MC7 (8.66-8.81 g/cm^3), the bottle density of fused corium was somewhat lower in MC8. In the first place, it is explained by a smaller urania content in the oxidic ingot.

2.4. SEM/EDX analysis of corium and steel

2.4.1. SEM/EDX analysis of corium sample from Pr1-MC8

The results of SEM/EDX analysis of the corium sample fused in Pr1-MC8 are given in Fig. 2.4.1 and Tab. 2.4.1. The crystallized corium microstructure is sufficiently uniform (see region 1 in Fig. 2.4.1) and consists predominantly of the $(U,Zr)O_2$ solid solution (see points P1, P2, P3 in Fig. 2.4.1, region 1-1 in Tab. 2.4.1).

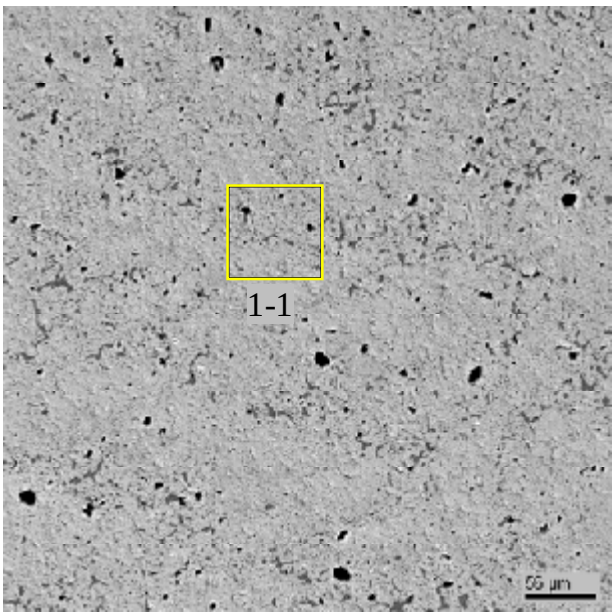

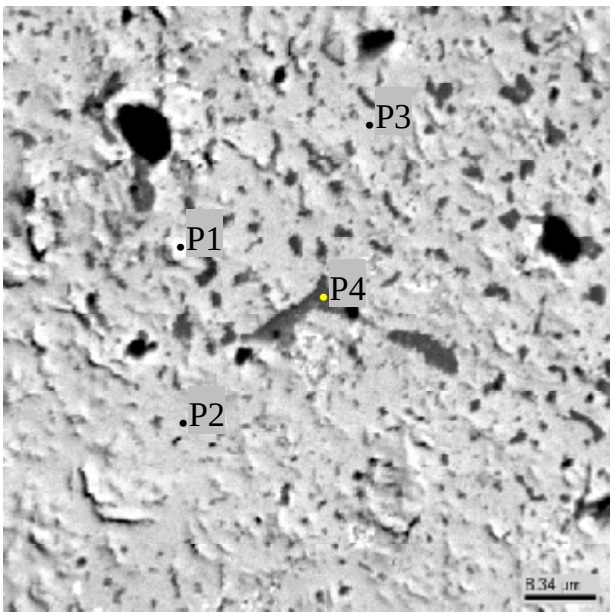

1(SQ1) 1-1

Fig. 2.4.1. Micrographs of corium sample from Pr1-MC8

Table 2.4.1

EDX results for corium sample from Pr1-MC8

No.		U	Zr	~O
SQ1	mass %	71.24	22.34	6.42
	mol. %	31.65	25.90	42.45
	mol. % MeO_x	55.00	45.01	
P1	mass %	73.54	25.00	1.46
	mol. %	45.81	40.64	13.55
	mol. % MeO_x	52.99	47.01	
P2	mass %	74.08	15.2	10.71
	mol. %	27.12	14.52	58.36
	mol. % MeO_x	65.12	34.88	
P3	mass %	76.19	15.06	8.75
	mol. %	31.01	15.99	53.00
	mol. % MeO_x	65.98	34.02	-
P4	mass %	11.23	88.78	-
	mol. %	4.62	95.38	-

In addition to the (U, Zr)O_2 solid solution, the presence of the α-Zr-based phase amounting to about 30 vol. % and containing some quantity of uranium may be noted (see point P4 in Fig. 2.4.1, region 1-1 in Tab. 2.4.1). Porosity of the corium sample amounted to about 3 vol. %. The bulk composition of the studied corium sample approximately corresponds to the specified stoichiometry of corium (see Fig. 2.4.1, region 1, SQ1 area in Tab. 2.4.1).

Therefore, it may be noted that the crust prototype consists of the (U,Zr)O_2 matrix with the α-Zr-based phase, sufficiently uniformly distributed in it.

2.4.2. SEM/EDX analysis of corium ingot from MC8

A template has been prepared from the ingot bottom part for the SEM/EDX analysis (Fig. 2.4.2).

Fig. 2.4.2. Corium template with regions marked for examination

Scanning of the said template up to the crust layer proves its high microstructural uniformity (see Fig. 2.4.3, region 1; Fig. 2.4.4, region 3; Fig. 2.4.5, region 4; Fig. 2.4.6, region 7) and compositional similarity of the crystallized corium (see Tab. 2.4.2, SQ1 area; Tab. 2.4.3, SQ1 area; Tab. 2.4.4, SQ1 area; Tab. 2.4.5, SQ1 area). Some microstructural changes in the ingot in comparison with microstructure of the sample from Pr1-MC8 (melting and crystallization of corium C-70 without interaction with the specimen) should be noted. These changes are expressed in the reduction of α-Zr quantity (compare Fig. 2.4.1, region 1-1 with Fig. 2.4.3, region 1-1 and Tabs. 2.4.1, 2.4.2). Also, it should be noted that in some regions iron was found in quantities at the lower threshold of EDX detection range (see Tab. 2.4.3, SQ1 area).

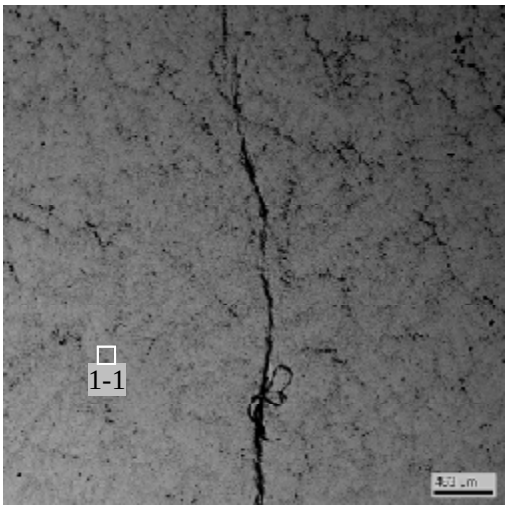

1(SQ1)

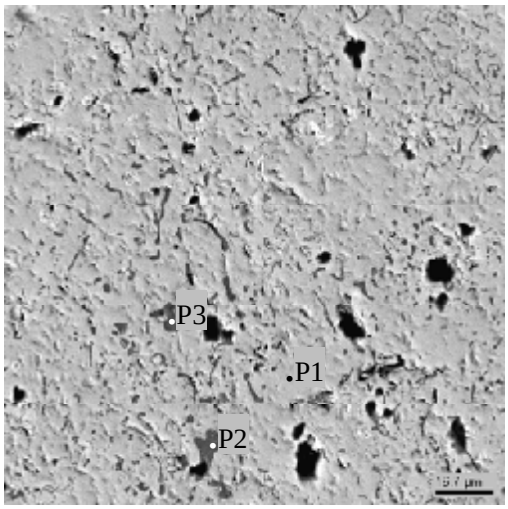

1-1

Fig. 2.4.3 Micrographs of region 1

Table 2.4.2

Data on region 1 EDX analysis

No.		U	Zr	~O
SQ1	mass %	57.19	18.14	24.68
	mol. %	12.13	10.03	77.84
	mol. % MeO_x	54.72	45.28	
P1	mass %	69.14	9.93	20.93
	mol. %	17.01	6.37	76.61
	mol. % MeO_x	72.75	27.25	

P2	mass %	9.0	81.58	9.42
	mol. %	2.49	58.79	38.72
	mol. % MeO_x	4.06	95.94	
P3	mass %	15.69	79.69	4.61
	mol. %	5.369	71.145	23.486
	mol. % MeO_x	7.017	92.983	

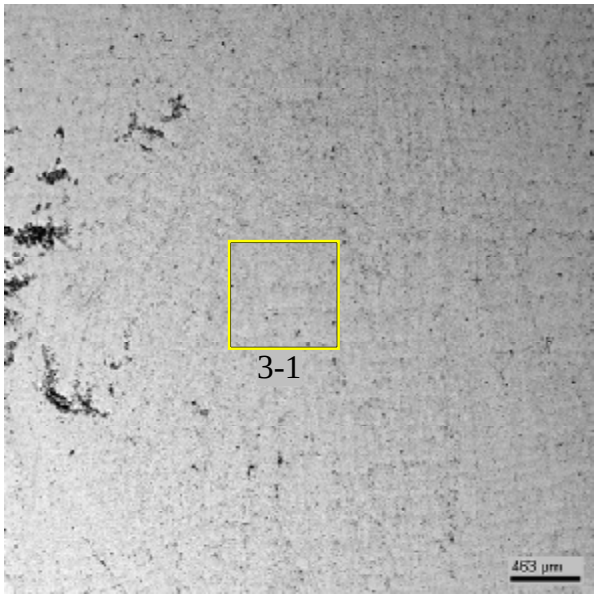

3

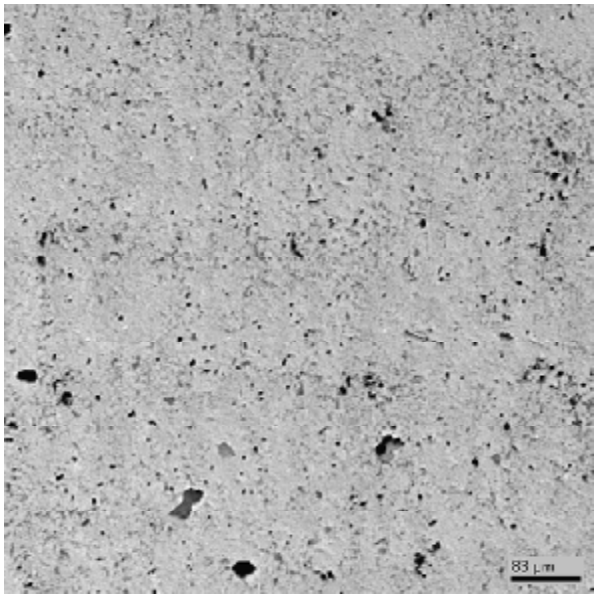

3-1(SQ1)

Fig. 2.4.4. Micrographs of region 3

Table 2.4.3

Data on region 3 EDX analysis

No.		U	Zr	Fe	~O
SQ1	mass %	53.54	17.33	0.31	28.82
	mol. %	10.12	8.55	0.25	81.08
	mol. % MeO_x	53.50	45.19	1.31	

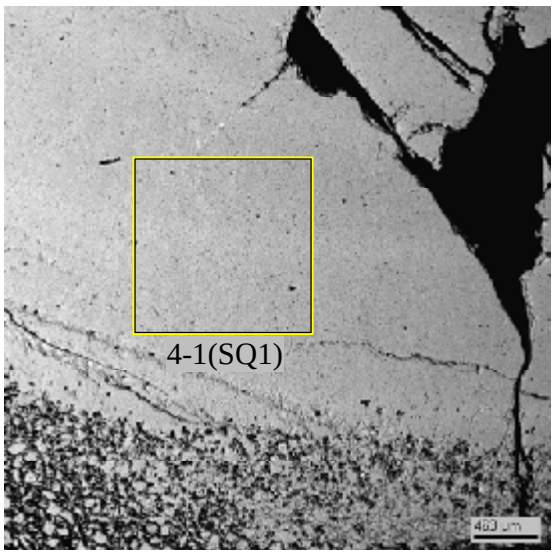

4

Fig. 2.4.5. Micrograph of region 4

Table 2.4.4

Data on region 4 EDX analysis

No.		U	Zr	~O
SQ1	mass %	59.61	15.16	25.23
	mol %	12.56	8.34	79.10
	mol. % MeO_x	60.11	39.89	

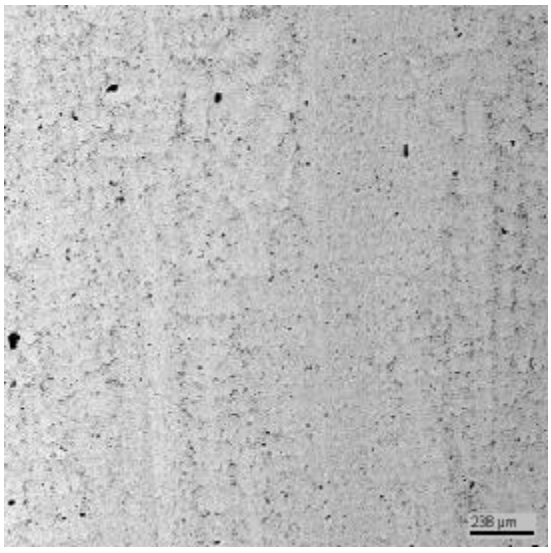

7(SQ1)

Fig. 2.4.6 Micrograph of region 7

Table 2.4.5

Data on region 7 EDX analysis

No.		U	Zr	~O
SQ1	mass %	60.08	18.06	21.86
	mol. %	13.89	10.89	75.21
	mol. % MeO_x	56.05	43.95	

The crust layer microstructure in MC8 was of layered type (e.g., Fig. 2.4.7), i.e. featured layers of the $U(Zr)O_2$ solid solution alternating with those composed of three phases: a) iron-based (see Fig. 2.4.7; Tab. 2.4.6, P2 point), b) $Zr(U)Fe_2$ intermetallide-based (see Fig. 2.4.7; Tab. 2.4.6, P1 point), and c) $U(Zr)Fe_2$ intermetallide-based ones (see Fig. 2.4.7; Tab. 2.4.6, P3 point).

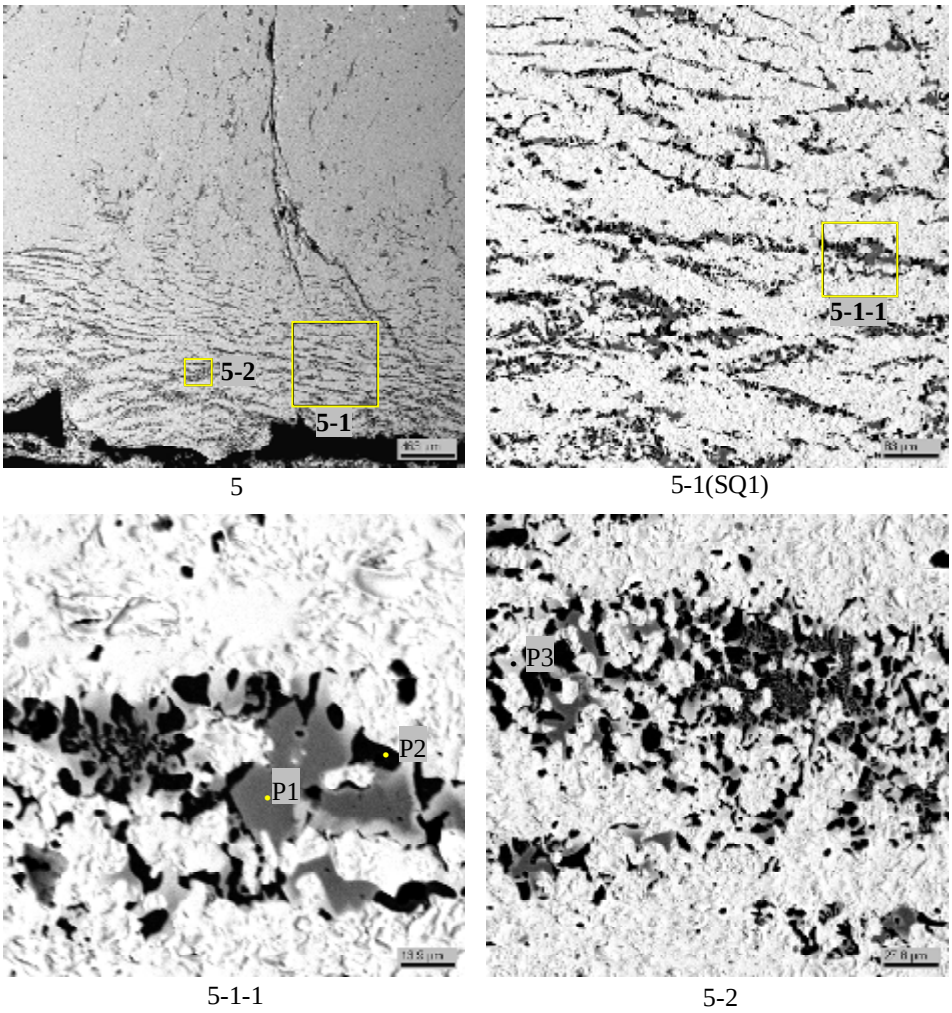

5 5-1(SQ1)

5-1-1 5-2

Fig. 2.4.7. Micrographs of region 5

Table 2.4.6

Data on region 5 EDX analysis

No.		U	Zr	Fe	Mn	Cr	Ni	~O
SQ1	mass %	62.47	5.61	16.57	-	0.63	-	14.71
	mol. %	16.91	3.96	19.12	-	0.78	-	59.23
	mol. % MeO_x	41.47	9.72	46.88	-	1.93	-	
P1	mass %	15.11	27.29	55.84	0.25	0.72	0.78	-
	mol. %	4.56	21.46	71.7	0.32	1	0.95	-
P2	mass %	0.72	-	92.99	0.26	2.95	0.78	2.3
	mol. %	0.16	-	88.25	0.25	3	0.7	7.64
	mol. % MeO_x	0.17	-	95.54	0.27	3.25	0.76	
P3	mass %	54.51	4.5	39.47	-	0.29	1.22	-
	mol. %	22.64	4.88	69.87	-	0.57	2.05	-

According to the EDX results, the crust layer with a layered structure contains about 17 mass % of steel components (see Fig. 2.4.7, Tab. 2.4.6, SQ1 area). Here and there the $Zr(U)Fe_2$ intermetallide-based phase occurs in the $U(Zr)O_2$ solid solution matrix as droplets (see Fig. 2.4.8, Tab. 2.4.7, P1 point). The content of iron in such zones amounts to about 12 mass % (see Fig. 2.4.8, Tab. 2.4.7; SQ1 area). There also occur non-layered zones which consist predominantly of the $U(Zr)O_2$ solid solution (see Fig. 2.4.9, region 2-2-1, Tab. 2.4.8, SQ2 area). In such zones the amount of iron was ~3-4 mass %.

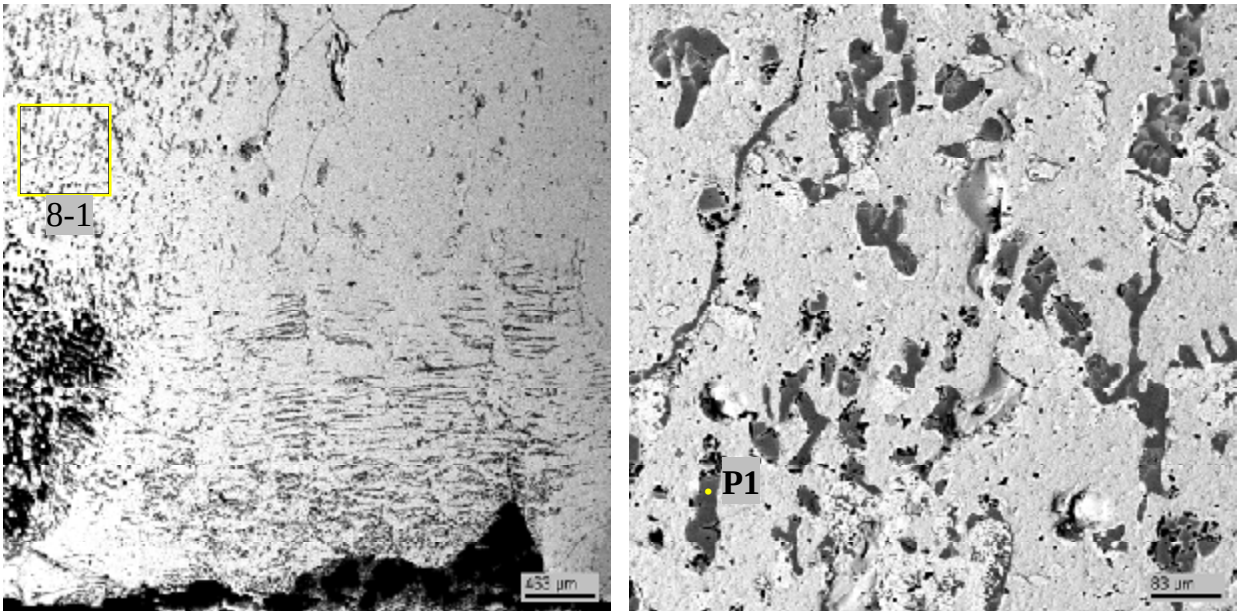

8 8-1 (SQ1)

Fig. 2.4.8. Micrographs of region 8

Table 2.4.7

Data on region 8 EDX analysis

No.		U	Zr	Fe	Cr	Ni	~O
SQ1	mass %	61.22	10.72	11.34	0.31	-	16.42
	mol. %	15.98	7.30	12.61	0.37	-	63.74
	mol. % MeO_x	44.07	20.14	34.78	1.01	-	
P1	mass %	15.44	30.14	52.69	0.66	1.06	-
	mol. %	4.74	24.12	68.89	0.93	1.32	-

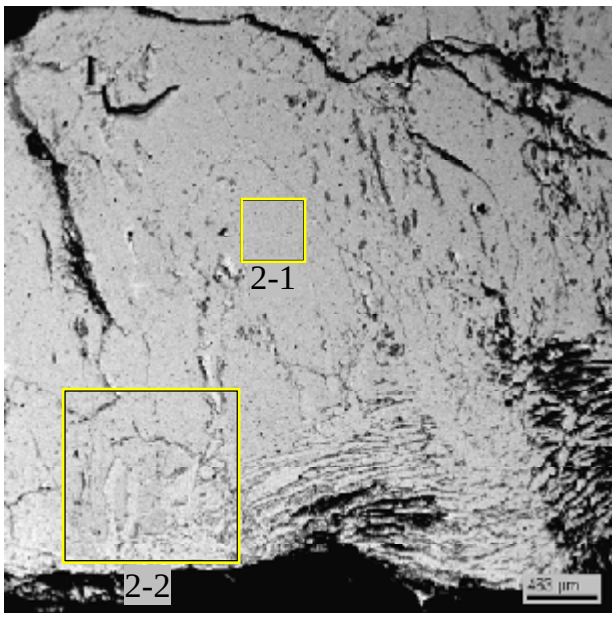

2

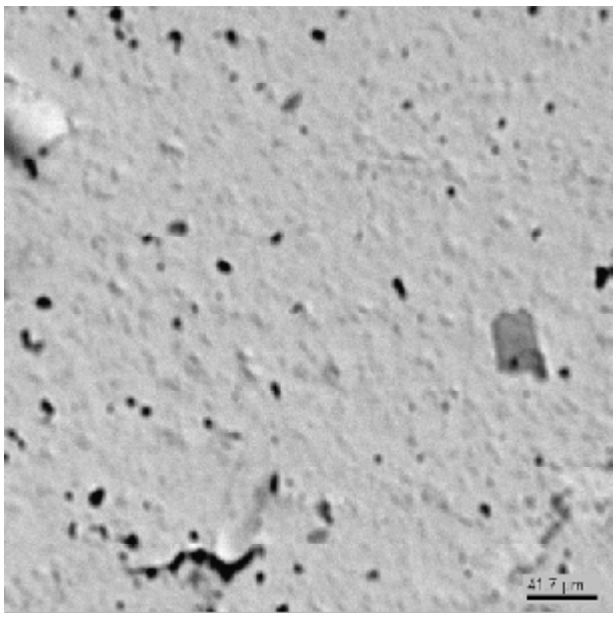

2-1(SQ1)

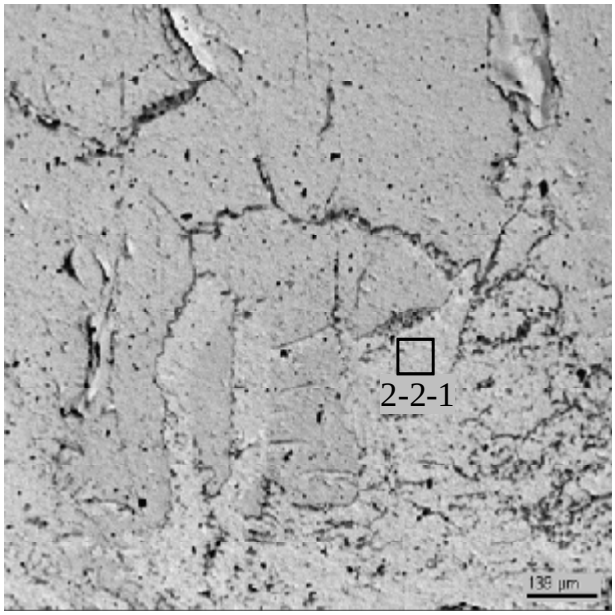

2-2

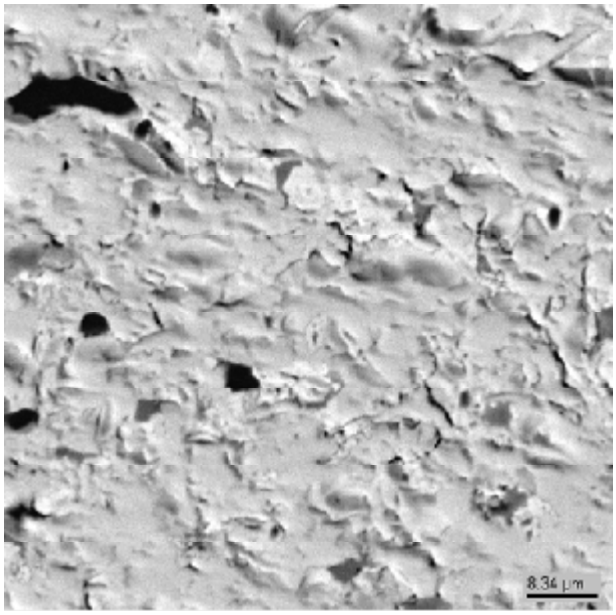

2-2-1(SQ2)

Fig. 2.4.9. Micrographs of region 2

Table 2.4.8

Data on region 2 EDX analysis

No.		U	Zr	Fe	~O
SQ1	mass %	63.46	12.446	1.241	22.85
	mol. %	14.38	7.36	1.199	77.06
	mol. % MeO_x	62.69	32.08	5.23	
SQ2	mass %	65.13	8.84	3.49	22.54
	mol. %	14.85	5.26	3.39	76.5
	mol. % MeO_x	63.2	22.37	14.43	

2.4.3. SEM/EDX analysis of the corium – steel specimen interaction zone

The zone of interaction between corium and the steel specimen is shown in Fig. 2.4.10. It reminds very much the interaction zone observed in MC6.

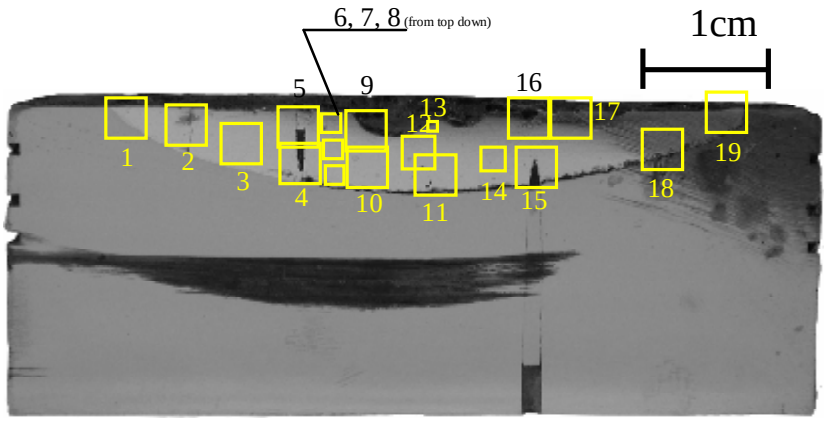

Fig. 2.4.10. Steel specimen template with regions marked for analysis

Microstructurally, the zone is dendritic, featuring iron dendrites with small amounts of chromium, nickel and manganese (see Fig. 2.4.11, Tab. 2.4.9, P2 point and Fig. 2.4.12, Tab. 2.4.10, P3 point) and eutectic interdendritic zones (see Fig. 2.4.13, region 2-1; Fig. 2.4.11, region 7-1-2; Fig. 2.4.14, region 9-1-1). Composition of the eutectic zones is given in Tabs 2.4.9 (SQ3), 2.4.11 (SQ1) and 2.4.12 (SQ1).

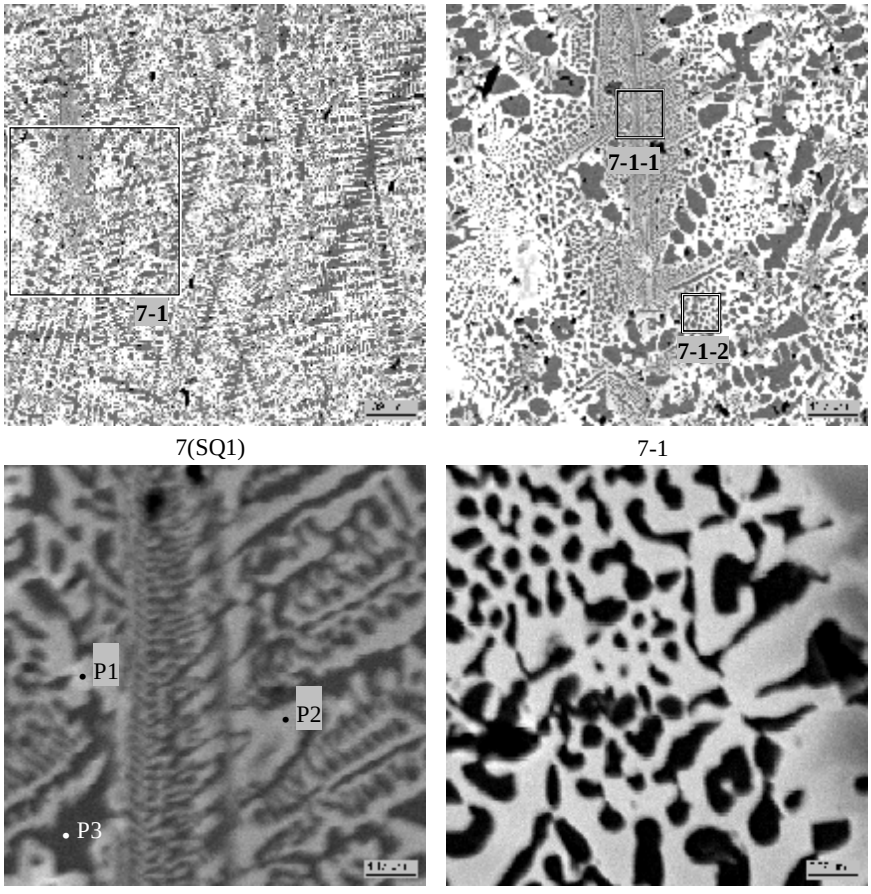

7(SQ1) 7-1

7-1-1(SQ2) 7-1-2(SQ3)

Fig. 2.4.11. Micrographs of region 7

Table 2.4.9

Data on region 7 EDX analysis

No.		**U**	**Zr**	**Fe**	**Cr**	**Ni**	**Mn**	**~O**
SQ1	mass %	21.95	6.28	69.02	1.63	0.79	0.32	-
	mol. %	6.37	4.76	85.36	2.17	0.92	0.41	-
SQ2	mass %	9.46	13.95	73.19	1.97	1.02	0.41	-
	mol. %	2.54	9.77	83.69	2.42	1.1	0.49	-
SQ3	mass %	37.52	3.68	56.53	1.02	1	0.25	-
	mol. %	12.6	3.22	80.88	1.57	1.36	0.37	-
P1	mass %	33.52	47.86	-	1.52	2.17	-	14.94
	mol. %	8.46	31.52	-	1.75	2.21	-	56.07
	mol. % MeO_x	19.25	71.72	-	3.99	5.03	-	
P2	mass %	20.75	16.52	60.31	1.09	0.96	0.37	-
	mol. %	6.26	13.01	77.58	1.49	1.17	0.49	-
P3	mass %	-	-	92.71	2.73	0.55	0.54	3.46
	mol. %	-	-	85.2	2.69	0.48	0.5	11.13
	mol. % MeO_x	-	-	95.87	3.02	0.54	0.56	

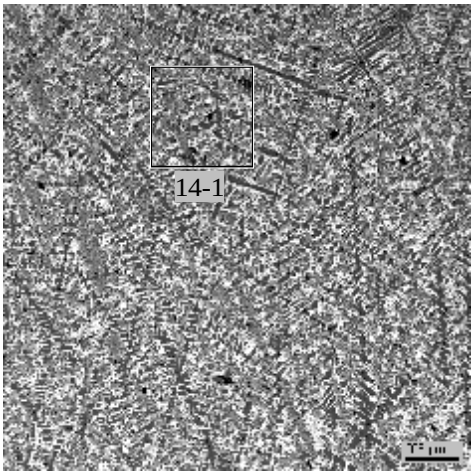

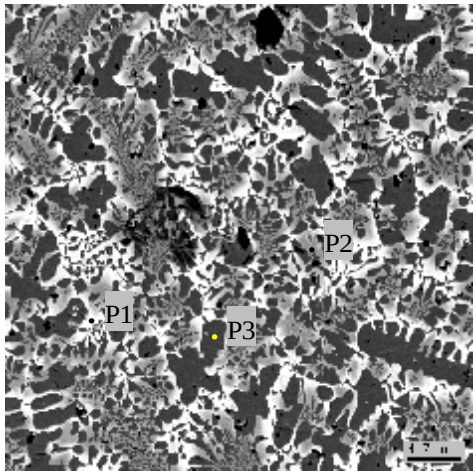

14(SQ1) 14-1

Fig. 2.4.12 Micrographs of region 14

Table 2.4.10

Data on region 14 EDX analysis

No.		U	Zr	Fe	Cr	Ni	Mn	~O
SQ1	mass %	20.01	6.73	70.15	1.8	0.87	0.44	-
	mol. %	5.71	5.01	85.36	2.35	1.01	0.56	-
P1	mass %	52.53	5.39	40.62	0.25	1.2	-	-
	mol. %	21.38	5.73	70.46	0.45	1.99	-	-
P2	mass %	13.93	15.86	67.25	1.61	0.89	0.43	0.03
	mol. %	3.92	11.65	80.7	2.07	1.02	0.53	0.11
	mol. % MeO_x	3.93	11.67	80.78	2.07	1.02	0.53	
P3	mass %	-	-	91.14	3.13	0.65	0.57	4.5
	mol. %	-	-	81.8	3.02	0.55	0.52	14.11
	mol. % MeO_x	-	-	95.23	3.51	0.64	0.61	

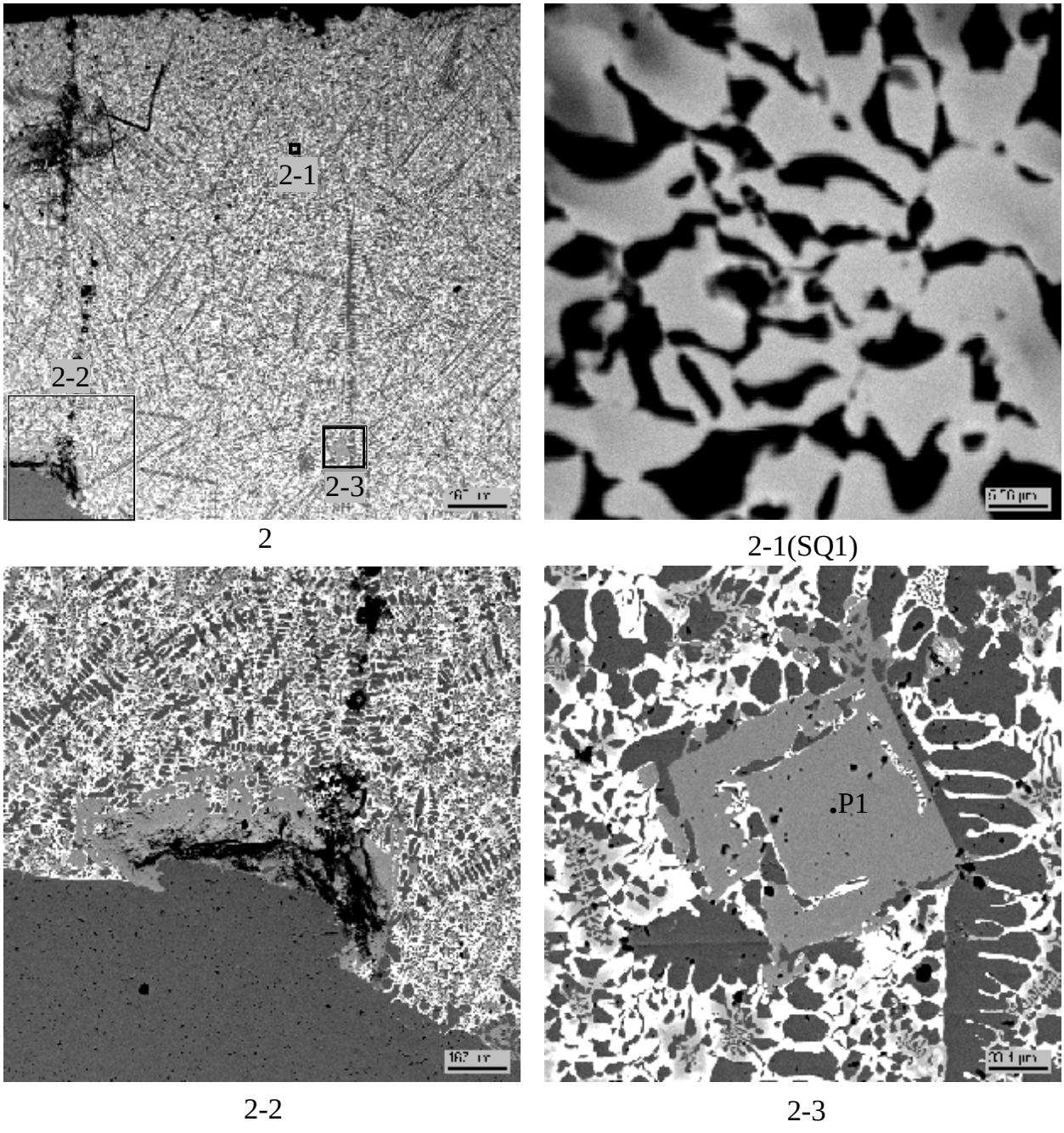

2 2-1(SQ1)

2-2 2-3

Fig. 2.4.13 Micrographs of region 2

Table 2.4.11

Data on region 2 EDX analysis

No.		U	Zr	Fe	Cr	Ni	Mn	~O
SQ1	mass. %	32.74	4.38	60.29	1.28	0.92	0.39	-
	mol. %	10.48	3.66	82.26	1.87	1.19	0.54	-
P1	mass. %	4.46	26.37	63.07	1.01	0.79	0.3	3.99
	mol. %	1.08	16.75	65.46	1.11	0.79	0.31	14.48
	mol. % MeO_x	1.27	19.59	76.55	1.31	0.91	0.37	

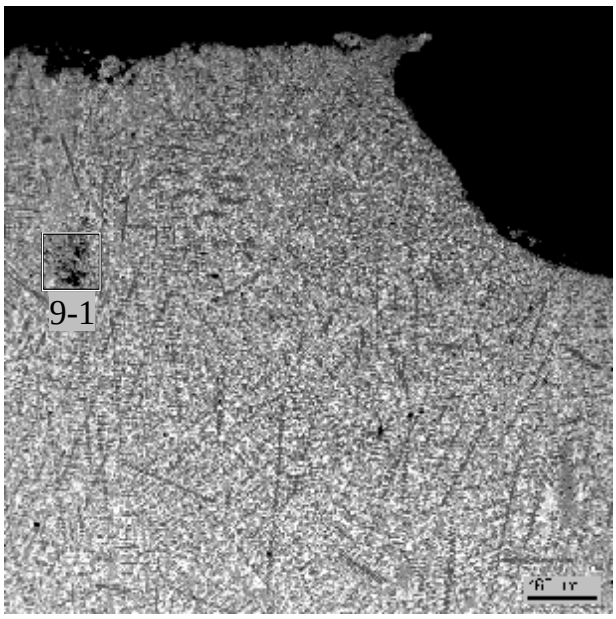

9

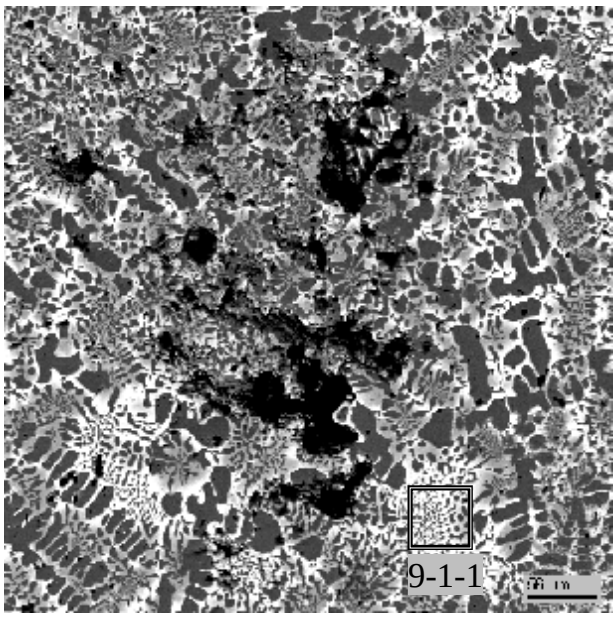

9-1

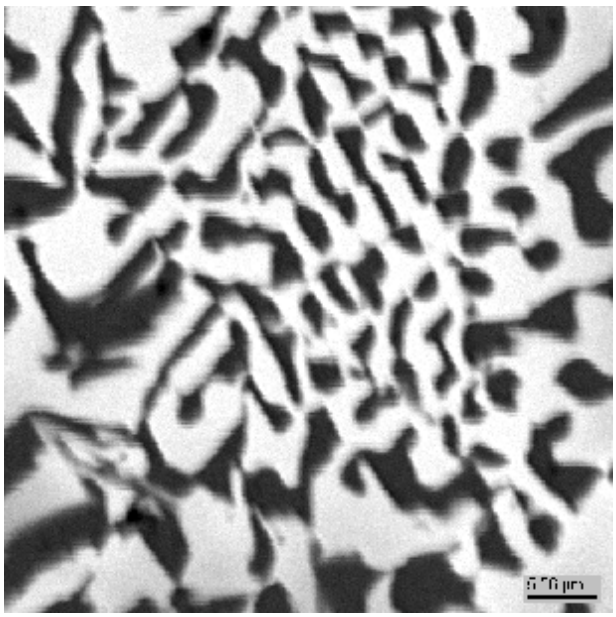

9-1-1 (SQ1)

Fig. 2.4.14. Micrographs of region 9

Table 2.4.12

Data on region 9 EDX analysis

No.		U	Zr	Fe	Cr	Ni	Mn	~O
SQ1	mass %	33.07	3.08	61.1	1.36	1.09	0.29	-
	mol. %	10.56	2.56	83.1	1.99	1.41	0.39	-

It should be noted that eutectic zones were similar in composition in different areas of the interaction zone. Insignificant compositional variations falling beyond the procedural error may be attributed to the capturing by the probe of dendrites and phases adjacent to the eutectic. The eutectic composition in different areas of the interaction zone are summarized in Tab. 2.4.13.

Table 2.4.13

Comparison of eutectic composition in different areas of the interaction zone

No.		U	Zr	Fe	Cr	Ni	Mn	~O
SQ1 (region 2)	mass %	32.74	4.38	60.29	1.28	0.92	0.39	-
	mol. %	10.48	3.66	82.26	1.87	1.19	0.54	-
SQ3 (region 7)	mass %	37.52	3.68	56.53	1.02	1	0.25	-
	mol. %	12.6	3.22	80.88	1.57	1.36	0.37	-
SQ1 (region 9)	mass %	33.07	3.08	61.1	1.36	1.09	0.29	-
	mol. %	10.56	2.56	83.1	1.99	1.41	0.39	-

Also it should be noted that the interaction zone features dendrites with a very fine microstructure (e.g., Fig. 2.4.11, region 7-1). Besides, noteworthy are the large cubic crystals of $Zr(U)Fe_2$ which have grown along the 'steel – interaction zone' boundary (more rarely inside the zone, but close to the boundary of steel) (see. Figs. 2.4.13, 2.4.15 - 2.4.21 and Tabs. 2.4.11, 2.4.14 2.4.16).

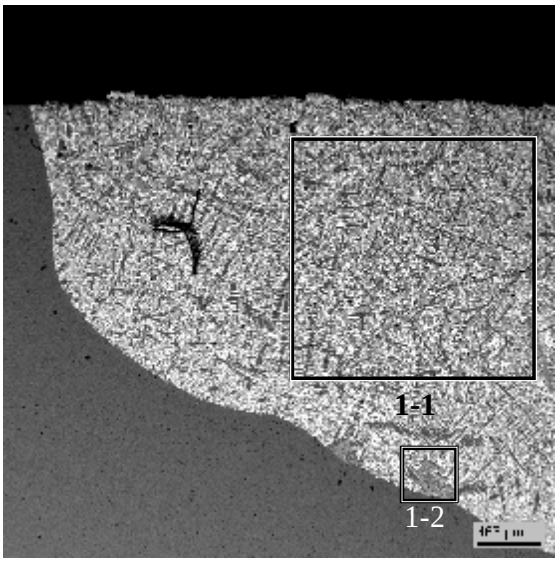

1

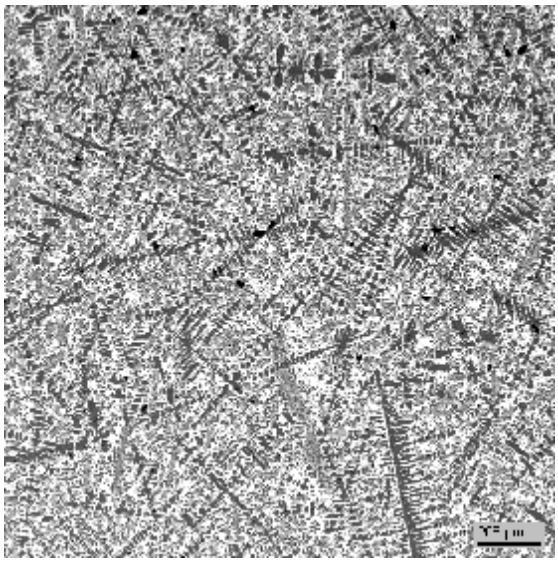

1-1(SQ1)

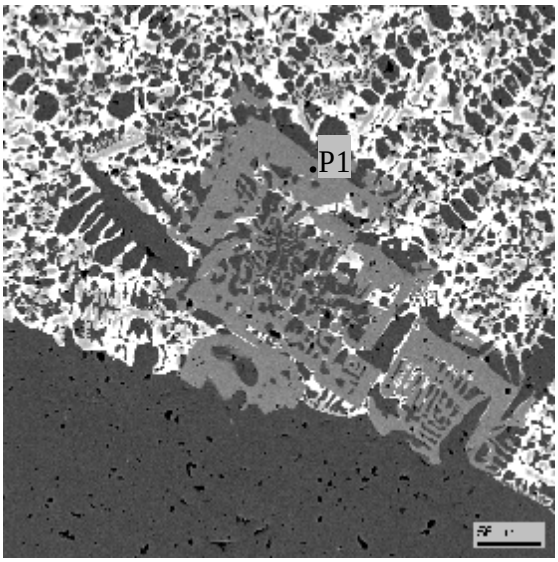

1-2

Fig. 2.4.15 Micrographs of region 1

Table 2.4.14

Data on region 1 EDX analysis

No.		U	Zr	Fe	Cr	Ni	Mn	~O
SQ1	mass %	21.37	6.69	68.12	1.92	1.15	0.27	0.48
	mol. %	6.09	4.97	82.71	2.51	1.33	0.34	2.04
	mol. % MeO_x	6.21	5.08	84.45	2.56	1.36	0.34	
P1	mass %	4.92	25.81	67	1.24	0.78	0.25	-
	mol. %	1.34	18.32	77.65	1.54	0.85	0.29	-

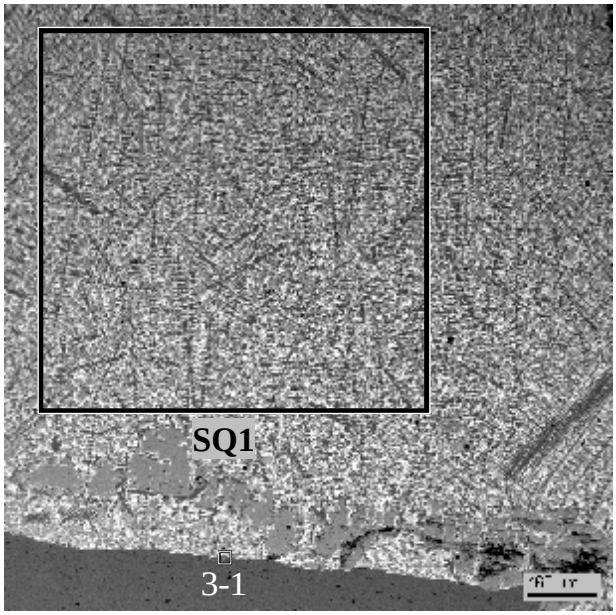

3

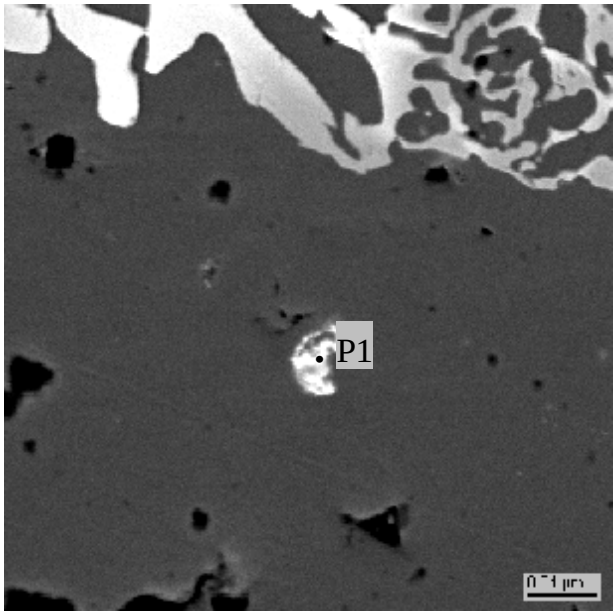

3-1

Fig. 2.4.16 Micrographs of region 3

Table 2.4.15

Data on region 3 EDX analysis

No.		U	Zr	Fe	Cr	Ni	Mn	~O
SQ1	mass %	22.11	6.14	68.45	2.02	0.95	0.33	-
	mol. %	6.42	4.66	84.71	2.68	1.12	0.41	-
P1	mass %	49.04	13.72	29.28	1.07	-	0.11	6.78
	mol. %	15.53	11.34	39.52	1.55	-	0.15	31.92
	mol. % MeO_x	22.81	16.65	58.05	2.27	-	0.22	

Studies of the interaction zone bulk composition in different regions shows compositional similarity across the whole interaction zone (see Figs. 2.4.15-2.4.25, Tabs. 2.4.14-2.4.20).

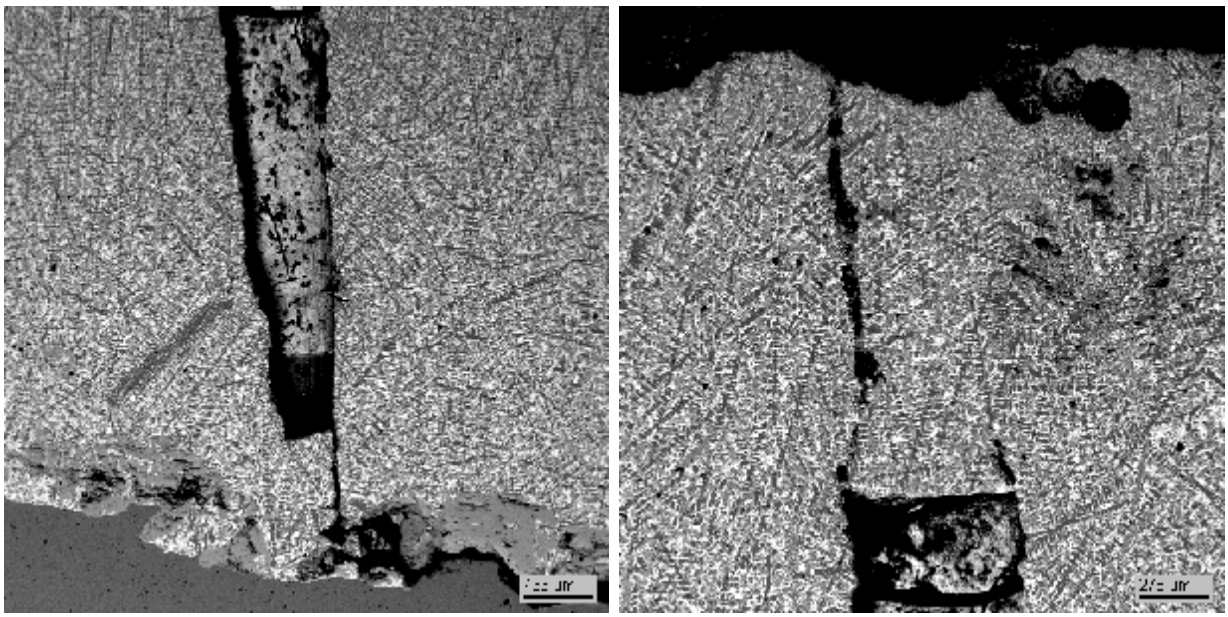

4 5

Fig. 2.4.17 Micrographs of regions 4 and 5

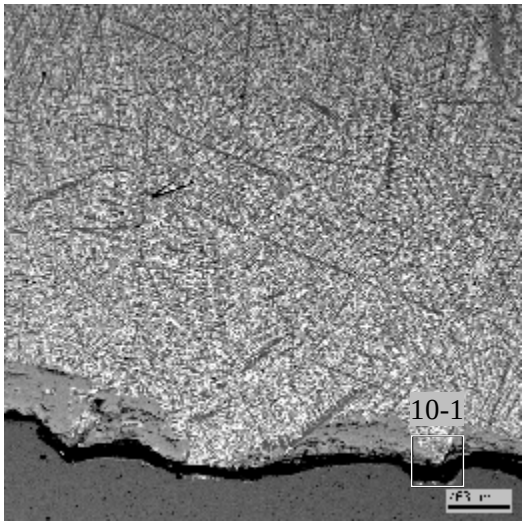

10

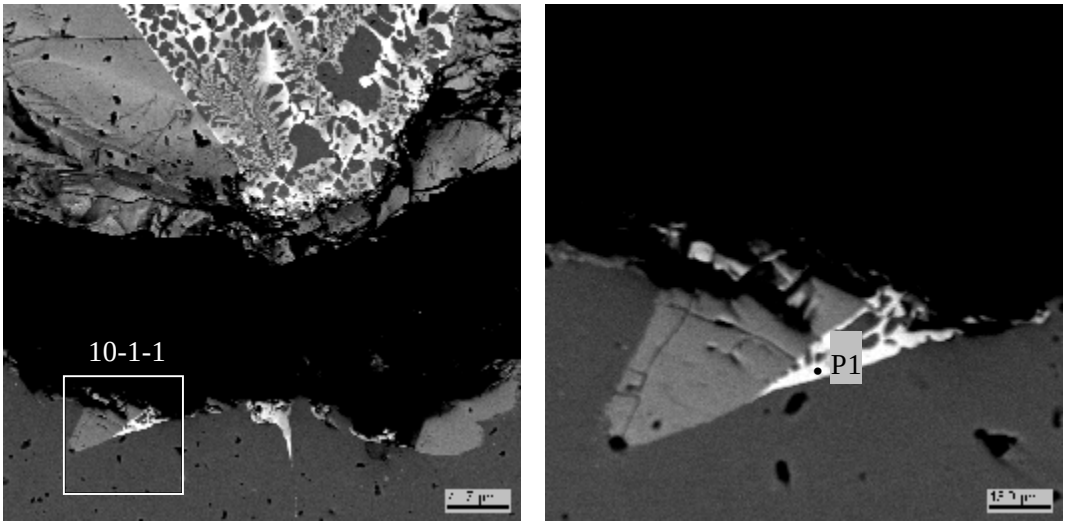

10-1 10-1-1

Fig. 2.4.18 Micrographs of region 10

Table 2.4.16

Data on region 10 EDX analysis

No.		U	Zr	Fe	Cr	Ni	~O
P1	mass %	58.19	2.66	38.02	-	1.13	-
	mol. %	25.11	2.99	69.93	-	1.98	-

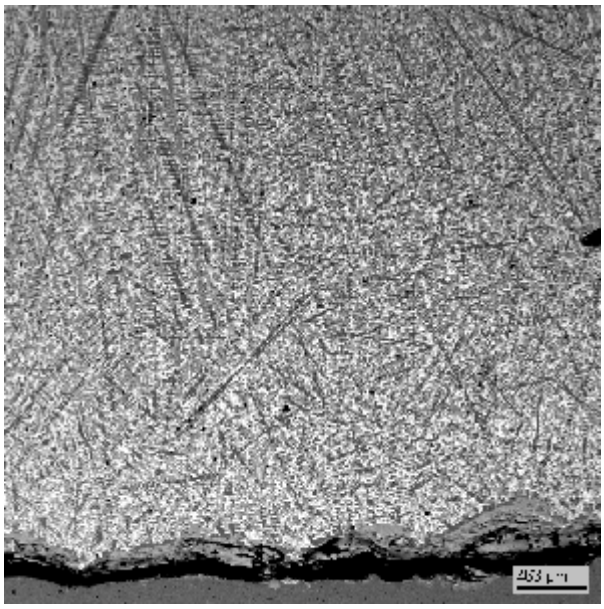

11

Fig. 2.4.19. Micrograph of region 11

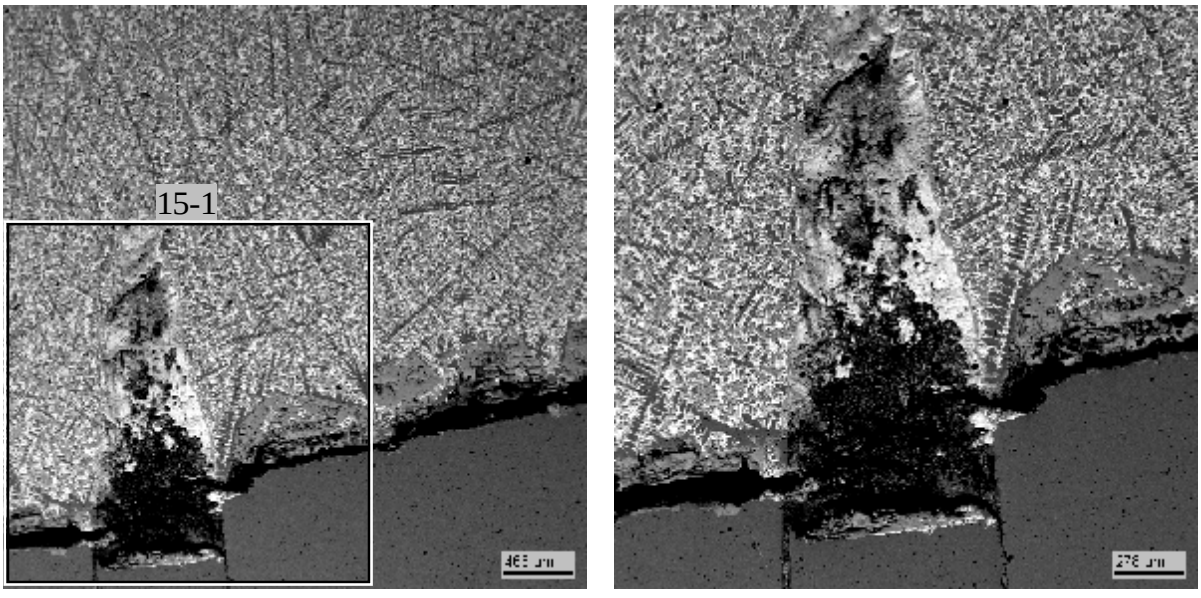

15 15-1

Fig. 2.4.20. Micrographs of region 15

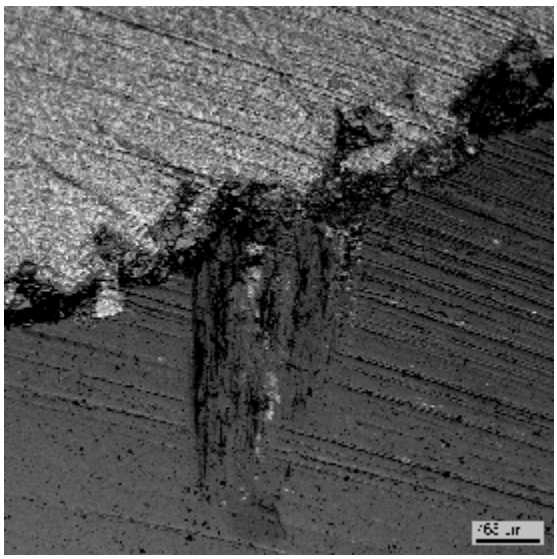

18

Fig. 2.4.21. Micrograph of region 18

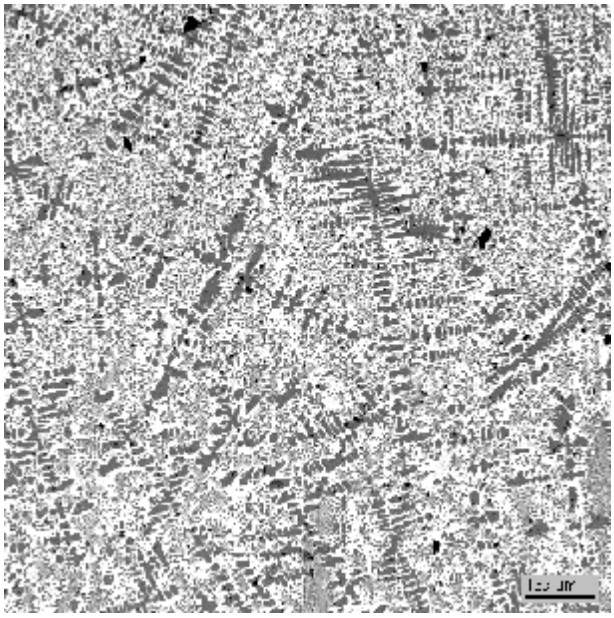

6(SQ1)

Fig. 2.4.22. Micrograph of region 6

Table 2.4.17

Data on region 6 EDX analysis

No.		U	Zr	Fe	Cr	Ni	Mn	~O
SQ1	mass %	21.88	7.91	67.08	1.8	0.92	0.41	-
	mol. %	6.4	6.04	83.55	2.4	1.09	0.53	-

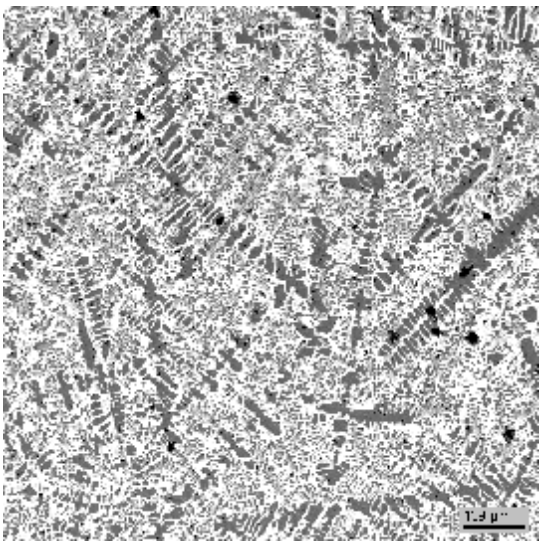

8 (SQ1)

Fig. 2.4.23. Micrograph of region 8

Table 2.4.18

Data on region 8 EDX analysis

No.		U	Zr	Fe	Cr	Ni	Mn	~O
SQ1	mass %	22.94	6.1	67.97	1.99	0.74	0.25	-
	mol. %	6.72	4.66	84.75	2.67	0.88	0.32	-

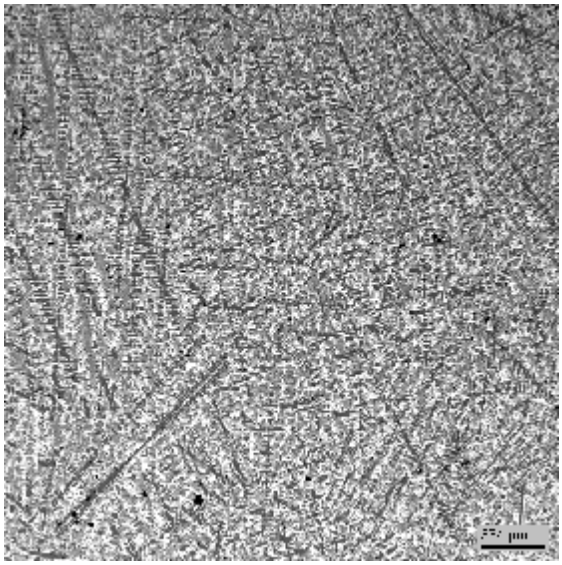

12

Fig. 2.4.24. Micrograph of region 12

Table 2.4.19

Data on region 12 EDX analysis

No.		U	Zr	Fe	Cr	Ni	Mn	~O
SQ1	mass %	22.01	6.11	66.75	1.85	0.9	0.45	1.93
	mol.%	6.03	4.36	77.93	2.32	1	0.53	7.83
	mol. % MeO_x	6.54	4.74	84.54	2.51	1.09	0.57	

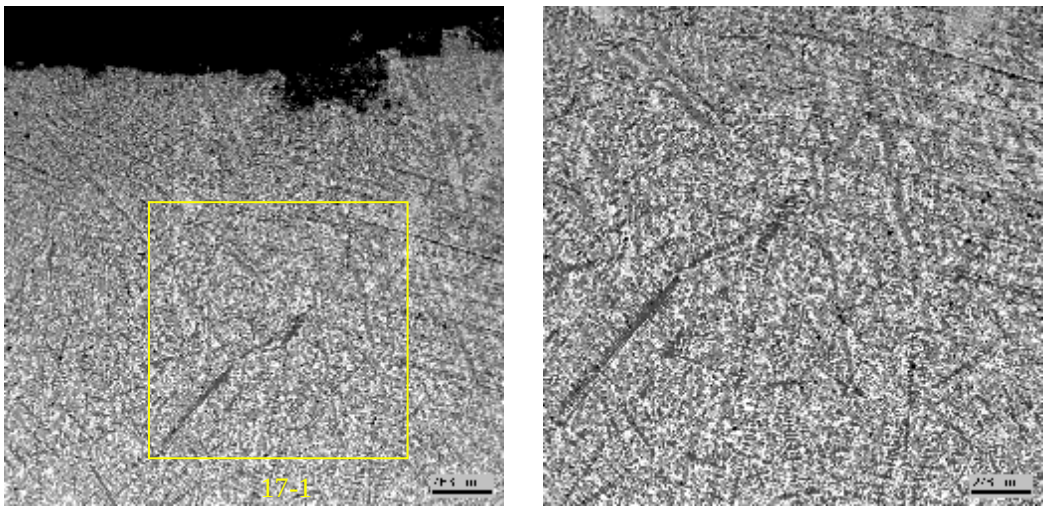

17 17-1(SQ1)

Fig. 2.4.25. Micrographs of region 17

Table 2.4.20

Data on region 17 EDX analysis

No.		U	Zr	Fe	Cr	Ni	Mn	~O
SQ1	mass %	23.48	6.56	66.36	1.81	1.22	0.35	0.23
	mol. %	6.87	5.01	82.78	2.43	1.44	0.45	1.02
	mol. % MeO_x	6.95	5.06	83.64	2.45	1.46	0.45	

Tab. 2.4.21 summarizes comparative data on bulk composition in all the examined regions of the interaction zone.

Table 2.4.21

EDX data on the interaction zone bulk composition

Regions		U	Zr	Fe	Cr	Ni	Mn	~O
1 SQ1	mass %	21.37	6.69	68.12	1.92	1.15	0.27	0.48
	mol. %	6.09	4.97	82.71	2.51	1.33	0.34	2.04
	mol. % MeO_x	6.21	5.08	84.45	2.56	1.36	0.34	
3 SQ1	mass. %	22.11	6.14	68.45	2.02	0.95	0.33	-
	mol. %	6.42	4.66	84.71	2.68	1.12	0.41	-
6 SQ1	mass. %	21.88	7.91	67.08	1.8	0.92	0.41	-
	mol. %	6.4	6.04	83.55	2.4	1.09	0.53	-
7 SQ1	mass. %	21.95	6.28	69.02	1.63	0.79	0.32	-
	mol. %	6.37	4.76	85.36	2.17	0.92	0.41	-
8 SQ1	mass. %	22.94	6.1	67.97	1.99	0.74	0.25	-
	mol. %	6.72	4.66	84.75	2.67	0.88	0.32	-
12 SQ1	mass. %	22.01	6.11	66.75	1.85	0.9	0.45	1.93
	mol. %	6.03	4.36	77.93	2.32	1	0.53	7.83
	mol. % MeO_x	6.54	4.74	84.54	2.51	1.09	0.57	
14 SQ1	mass. %	20.01	6.73	70.15	1.8	0.87	0.44	-
	mol. %	5.71	5.01	85.36	2.35	1.01	0.56	-
17 SQ1	mass. %	23.48	6.56	66.36	1.81	1.22	0.35	0.23
	mol. %	6.87	5.01	82.78	2.43	1.44	0.45	1.02
	mol. % MeO_x	6.95	5.06	83.64	2.45	1.46	0.45	

2.5. Specimen metallography

These studies pursued three objectives: 1) pre-test inspection of steel; 2) determination of the ablation depth of steel thermochemically influenced by corium; 3) investigation of steel macro- and microstructure off the interaction boundary into the specimen.

2.5.1. Pre-test inspection of steel

The specimen for MC8 was made from 15Kh2NMFA-A vessel steel produced by Izhorskiye Zavody Association for a VVER-1000.

Like for MC5, MC6 and MC7, a blank was flame cut from a reactor vessel fragment for MC8 and used for producing a specimen for the test and a witness specimen. Pre-test inspection of the witness specimen included elemental analysis by XRF and microhardness measuring.

The main steel components content determined by XRF has proved conformity of the steel with Specs. 108-765-78 for the vessel steel 15KhNMFA-A (see Tab. 2.3.3).

The value of microhardness was determined from 5 imprints. The integral microhardness value for the reference specimen was H_{μ} = 250 – 260.

Dimensions of the specimen before the test were measured from the upper top and from the grooves cut in the cylindrical surface. The measurements were performed with the calipers with a scaling factor of 0.02 mm and the MBC-9 stereoscopic microscope with a 14 μm scaling factor and x50 magnification.

Fig. 2.5.1a shows the distance A from the upper top to the first groove, distance B to the reference hole (acoustic defect) and diameter D of the reference hole. The data obtained from four measurements made in the opposed points of the specimen (Fig. 2.5.1.b) are summarized in Tab.2.5.1.

Table 2.5.1

Steel specimen measurements

A_1	A_2	A_3	A_4	B_1	B_2	D_1	D_2
mm							
3.27	3.28	3.25	3.28	5.19	5.25	2.12	2.051

Specimen length L = 104.20 mm.

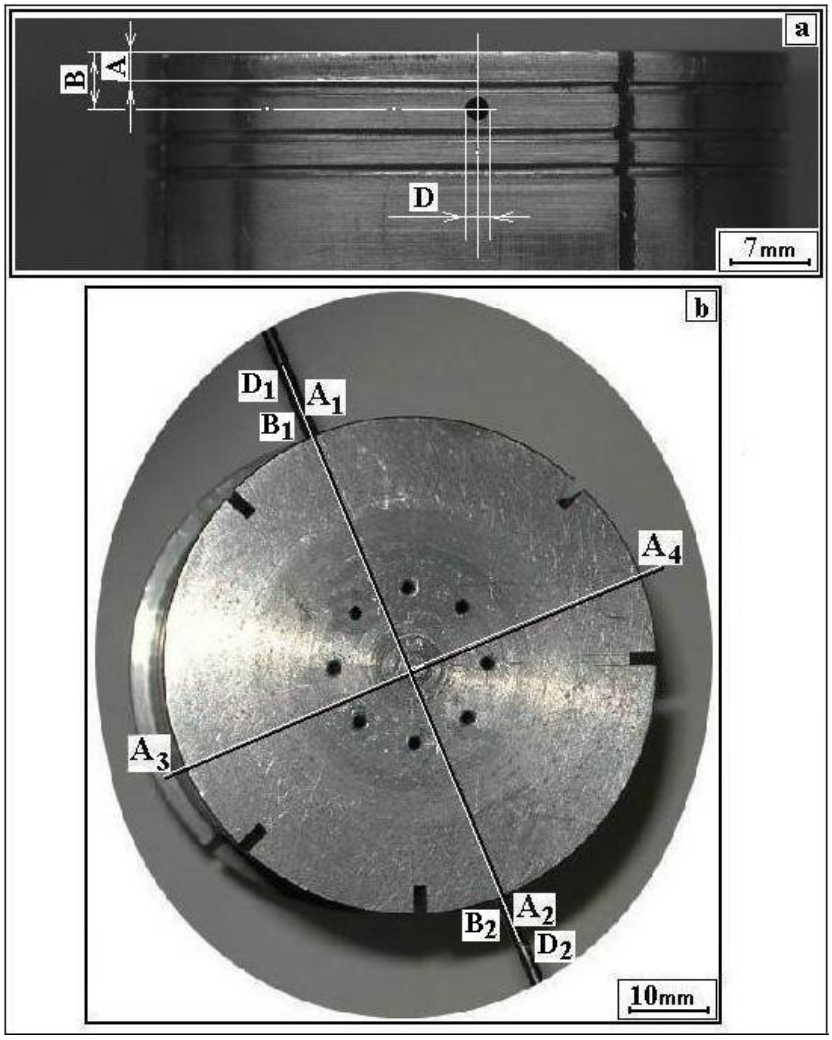

Fig. 2.5.1. Fragments of steel specimen lateral surface (a) and upper top (b) before MC8

A (A_1, A_2, A_3, A_4), B (B_1, B_2), D (D_1, D_2)- points of check measurements.

2.5.2. Determination of steel ablation depth

After the test the corium ingot and vessel steel specimen were embedded in epoxy in order to prevent destruction of the corium ingot and breaking of the steel specimen edges when cutting it and preparing thin sections. The produced blocks were cut along the axis in the plane perpendicular to the reference hole axis. All measurements were made on the specimen longitudinal section. The specimen upper top and the place of longitudinal section are shown in Fig. 2.5.2. A view of the template with regions marked for examination is given in Fig. 2.5.4.

The depth of ablation was directly measured using the microscope of the PMT-3 microhardness tester at x180 and x487 magnifications, and the MBC-9 stereoscopic microscope at x50 and x100 magnifications. The scale factor of micrometer screws and object plate of microhardness tester is 0.01 mm. The measurement error is ±10 μm; it was determined with stage micrometer. The scanner-produced image of a macrosection was processed on the computer and a profilogram of the surfaces of the corium – U-Zr-Fe-O alloy (interaction zone) – steel interfaces in the specimen axial cut plane has been plotted (Fig. 2.5.3.). According to the results of specimen measuring before and after the test, the maximum deepening of the interaction zone upper boundary (2) relative to the initial top amounted to 2.13 mm, while the interaction zone spreads to a depth of 6.65 mm (Fig. 2.5.3.).

1 – specimen cutting plane

Fig. 2.5.2. Specimen upper top after MC8

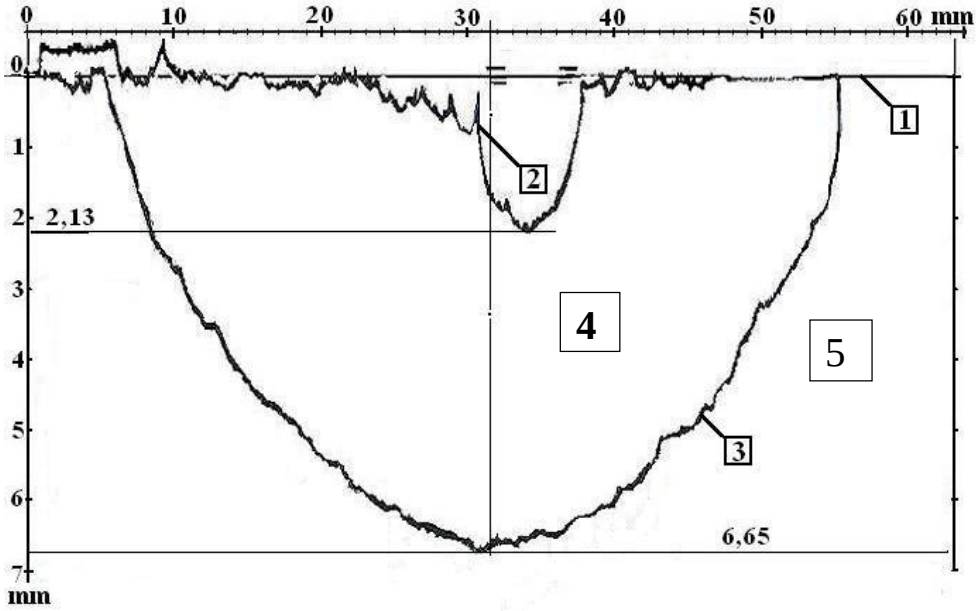

1 – position of the initial top plane; 2 – oxides – interaction zone boundary; 3 – steel specimen - interaction zone boundary; 4 - interaction zone; 5 – steel.

Fig. 2.5.3. Profilogram of the interface surfaces: corium – U-Zr-Fe-O alloy (interaction zone) – steel, in the specimen axial cut plane

2.5.3. Steel macro- and microstructure

Macro- and microstructure of the specimen were assessed using a template from the longitudinal section of the steel specimen upper part (Fig. 2.5.4). Grinding and polishing of the specimen was done according to the standard technique. To reveal the microstructure, the prepared section was treated with etchants for the austenitic and pearlitic steels [15].

The section surface was photographed at x25 magnification by a NIKON digital camera coupled with the METALLUX metallographic microscope at x200, x400 and x800 magnifications.

The section clearly shows the interaction zone which is visible in Fig. 2.5.3 (above the interaction boundary). A chain of gas pores was discovered along the interaction zone boundary, and in the central part the interaction zone was found detached from steel (Fig. 2.4.18, Fig. 2.4.19). Below the interaction zone lower boundary, steel microstructure features numerous fine pores down to a depth of 2 mm (Fig. 2.4.15).

Down to a depth of 3 mm below the interaction boundary, steel microstructure is composed of large ferrite isolates (Fig. 2.5.4.) with 0.02 % carbon content [15].

Such a structure indicates heating above the critical point $Ac_{3,}$ total recrystallization of steel and development of the processes of carbon and chromium diffusion at the expense of a high temperature gradient along the specimen height.

The microstructure of metal to a depth of 25 mm from the initial top plane of the specimen may be regarded as a conjugated system of steels with different content of carbon and alloying elements. Basically, there occurred formation of a ferrite-pearlitic structure (Fig. 2.5.4), which may form at a relatively high cooling rate of the steel heated above the critical point Ac_3 (from the austenitic state).

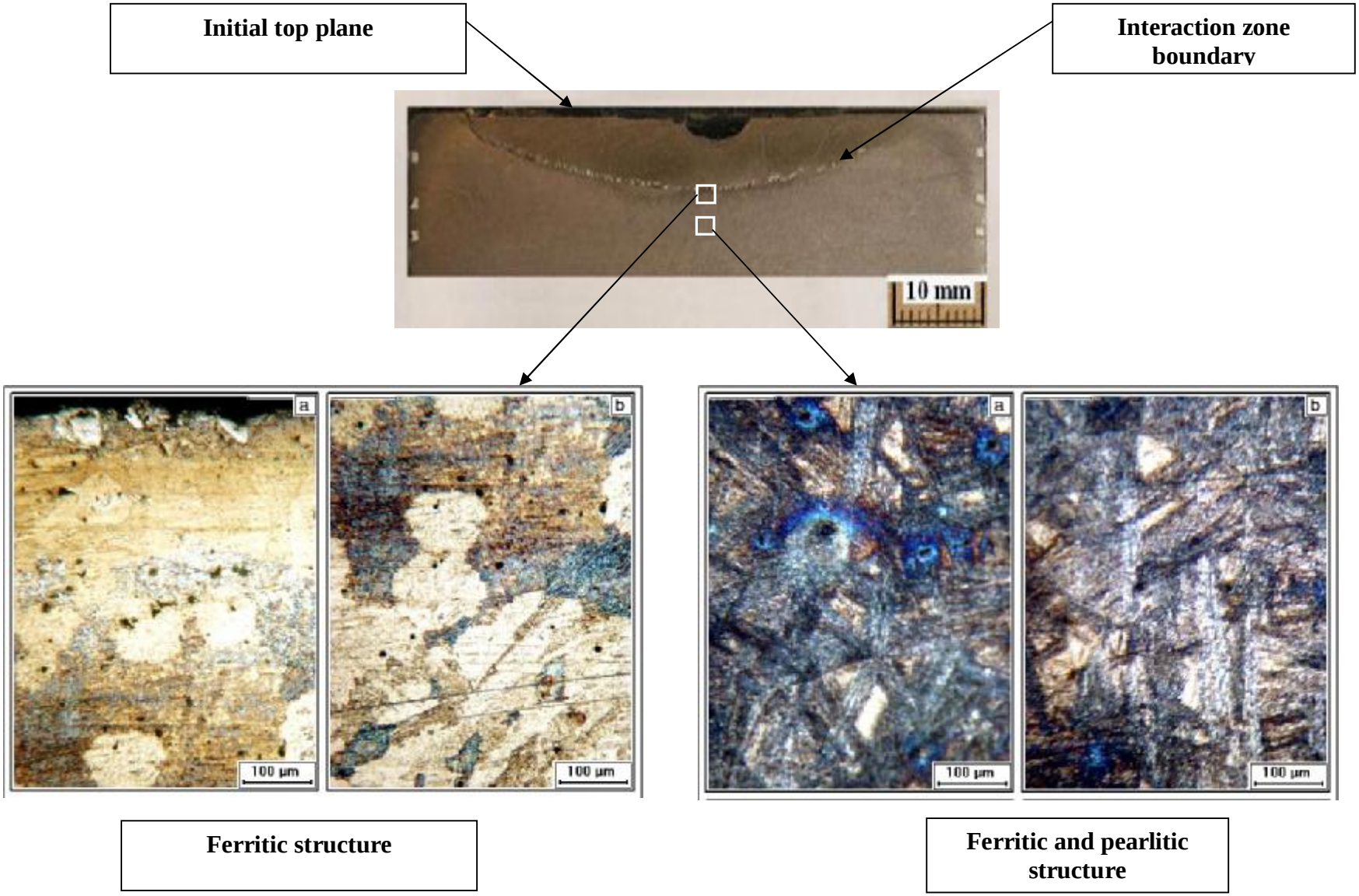

Fig. 2.5.4. Steel microstructure in the marked regions below the interaction boundary

2.6. Differential thermal analysis

The differential thermal analysis (DTA) of a sample from the interaction zone of MC8 was made by the SETSYS Evolution-2400 analyzer.

The temperature of steel specimen - corium interaction initiation (solidus temperature, T_{sol}) was determined by the start of the endothermic effect at the sample heating and by the start of the exothermic effect at its cooling, the second was somewhat lower than the first. The difference in T_{sol} values is explained by a possible sample subcooling below T_{sol} during cooling, whereas there has not been detected any substantial superheating of a solid body above the solidus point in our numerous tests. Therefore we consider the value registered at heating the sample as more credible.

Tab.2.6.1. offers the eutectic composition from the interaction zone according to the SEM/EDX analysis.

Table 2.6.1

SEM/EDX data on the eutectic composition

No.		U	Zr	Fe	Cr	Ni	Mn
Eut	mass %	37.52	3.68	56.53	1.02	1	0.25
	mol. %	12.6	3.22	80.88	1.57	1.36	0.37

Figs. 2.6.2.-2.6.3. show thermograms of the sample from the interaction zone.

DTA conditions: sample mass – 28 mg; carrier gas – argon; carrier gas flow rate – 4 ml/min; heating rate – 5°C/min; thermocouple type – B (Pt-30% Rh /Pt- 6% Rh)

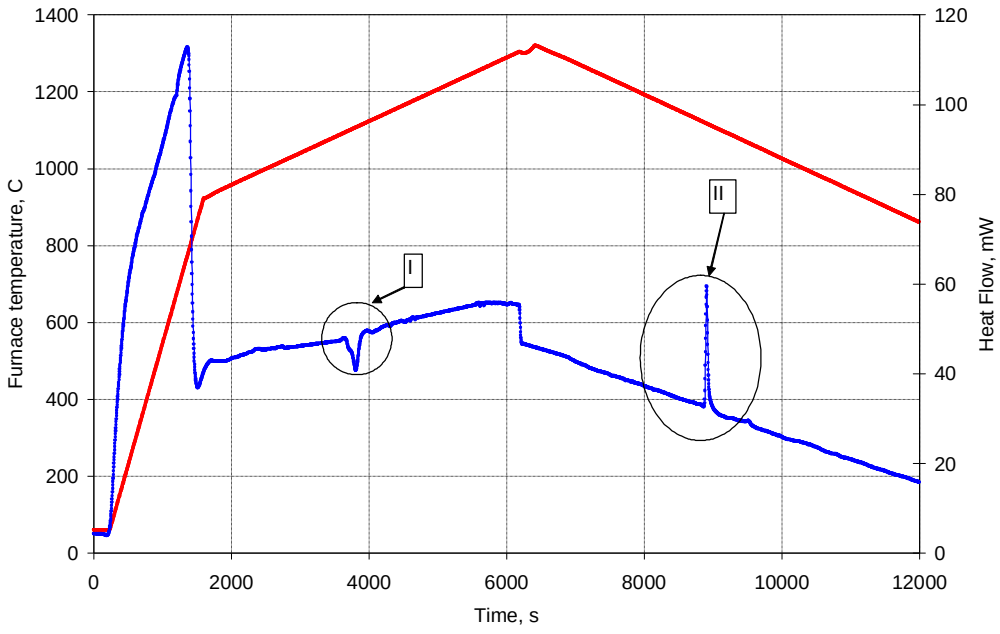

Fig. 2.6.2. Thermogram of the sample

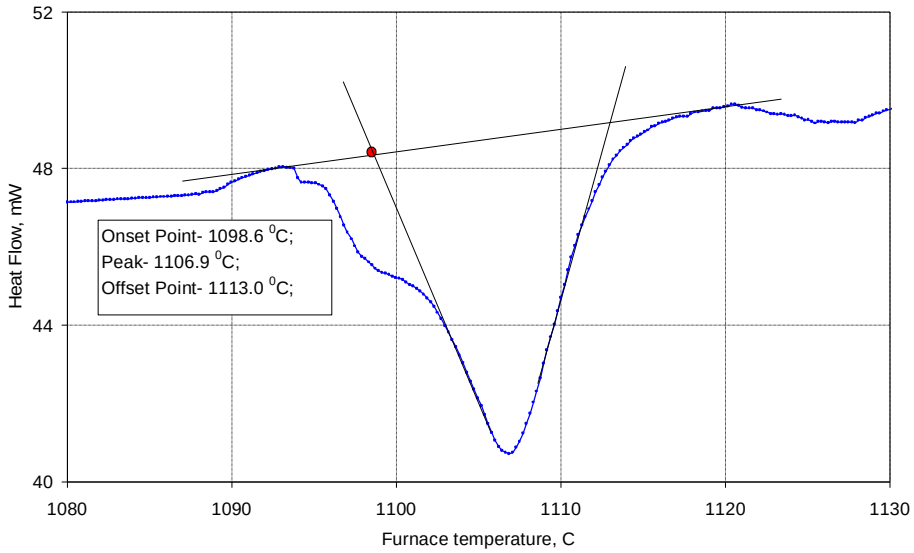

Fig. 2.6.3. Termogram of the sample, enlarged fragment

Fig. 2.6.3 demonstrates distinct peak with the endothermic effect between 1097 – 1113°C. In order to determined the temperature corresponding to the peak start, the baseline "linear from first to last point" was chosen, after which tangent lines to the peak slopes were drawn. The intersection of base and tangent lines yielded T_{sol} of 1098.6°C.

3. Discussion of results

In MC6 and MC7, molten corium composition corresponded to ~C-30, and the time of its interaction with vessel steel specimens was around 10 hours. The main difference of MC7 from MC6 is in the maintenance of the maximum temperature at the corium – specimen upper top interface at about 1150ºC, while in MC6 this temperature was maintained at ~1400ºC. In contrast to these tests, corium ~ C-70 was used in MC8, while the temperature maintained at the interface was similar to that in MC6. Fig. 3.1 shows diametrical cuts (templates) with marked boundaries of the vessel steel – corium interaction zones from MC6, MC7 and MC8.

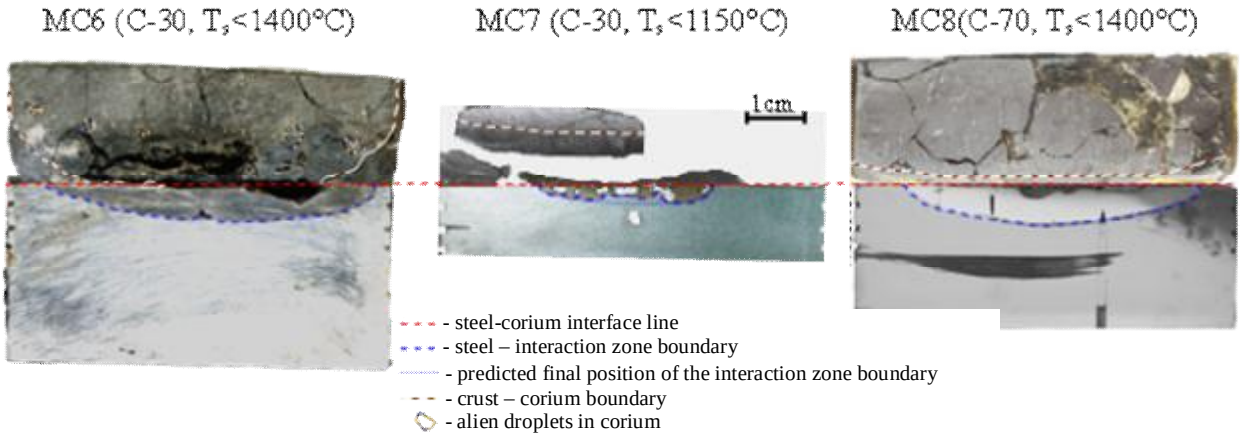

Fig. 3.1. Diametrical cuts (templates) of ingots from MC6, MC7 and MC8

The analysis of ingot templates leads to the following conclusions:

- an area of degenerated steel (interaction zone) is observed in all three ingots;
- the interaction zone is somewhat asymmetrical relative to the axis of ingots from MC6 and MC8, though the boundary with steel is sufficiently even and, most likely, corresponds to the position of some isotherm which is critical for the given system. In the ingot from MC7, the boundary of interaction with steel represents a complex surface. However, the US measurements allow a supposition about the insufficiency of exposure time, and a prediction concerning the ultimate position of the boundary in the opposite case (see Fig. 3.1);
- the interaction zone in MC6 and MC8 is monolithic, while in MC7 it is porous. On the other hand, in both MC6 and MC8 there is a quite big porous space between the interaction zone and crystallized corium, which is not observed in MC7;
- the SEM/EDX analysis of interaction zones has shown that in MC6 it is a homogeneous dendritic crystallized melt, and in MC8 – a homogeneous dendritic crystallized melt with included crystals of the $Zr(U)Fe_2$ intermetallide. In the case of MC7, it is a melt very close to the eutectic and, hence, a picture of crystallization that is typical for crystallization of eutectic melts has been observed. In addition to the eutectic, crystalline inclusions of the $Zr(U)Fe_2$ intermetallide and a monocrystalline layer of the $U(Zr)Fe_2$ intermetallide were found.;
- the corium part of the ingot from MC6 contained steel inclusions which were missing in the ingots from MC7 and MC8. The layered structure of the crystallized crust layer in MC8 also should be noted (see Fig. 3.2).

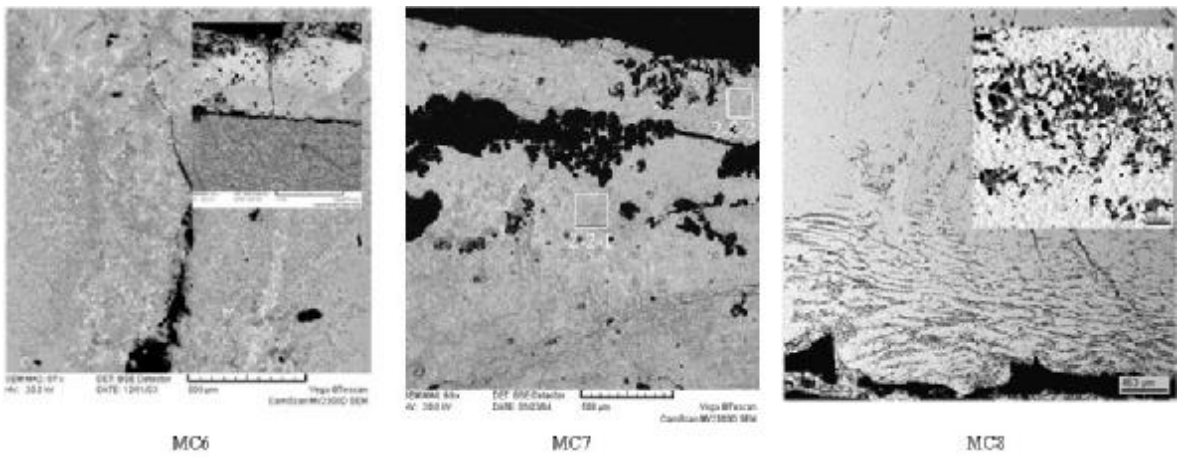

Fig. 3.2. Crust layers from MC6, MC7 and MC8

Since in MC6 – MC8 the presence of such intermetallide compounds as UFe_2 and $ZrFe_2$ was registered in the interaction zone, analysis of the processes occurring at the interaction of corium with steel requires data on phase equilibriums in the UFe_2-$ZrFe_2$-Fe system.

Literature sources contain experimental data on phase diagrams of the U-Fe and Zr-Fe systems (see Figs. 3.3 and 3.4, respectively).

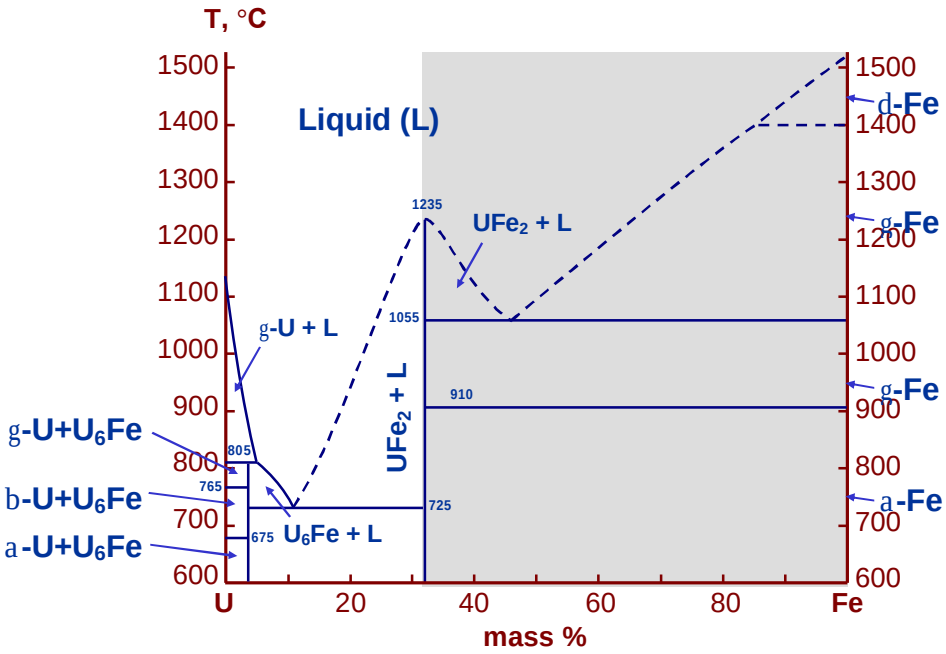

Fig. 3.3. Diagram of the U-Fe system [16, 17]

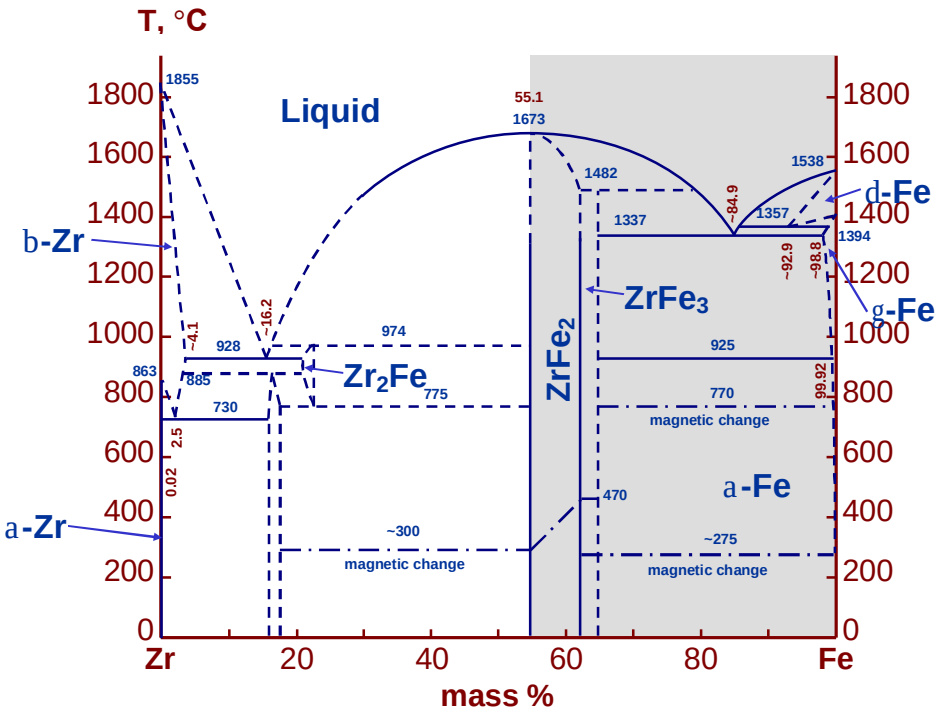

Fig. 3.4. Diagram of the Zr-Fe system [18]

For the UFe_2-$ZrFe_2$ system, only the melting temperatures of pure substances are known. Therefore, a phase diagram has been calculated and constructed for the subsequent analytical purposes. Besides the melting temperatures of pure substances, the diagram construction requires data on entropies of their melting, which have been calculated on the basis of the Richards' rule, according to which the entropy of ionic crystals melting is a constant and equals 8.8 J/(mol.·K). The limit values of components solubility (points of the diagram) were determined experimentally (MC8 test). The results of diagram calculation in approximation to the regular solutions model are presented in Figs. 3.5 and 3.6.

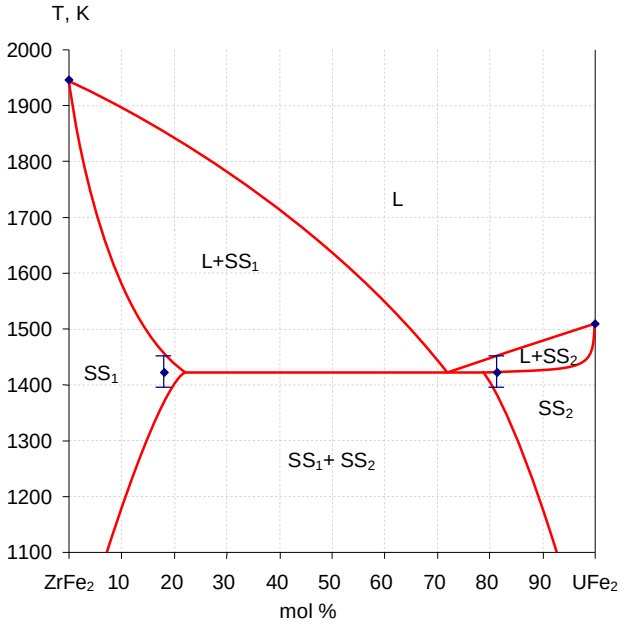

Fig. 3.5. Diagram of the $ZrFe_2$-UFe_2 system

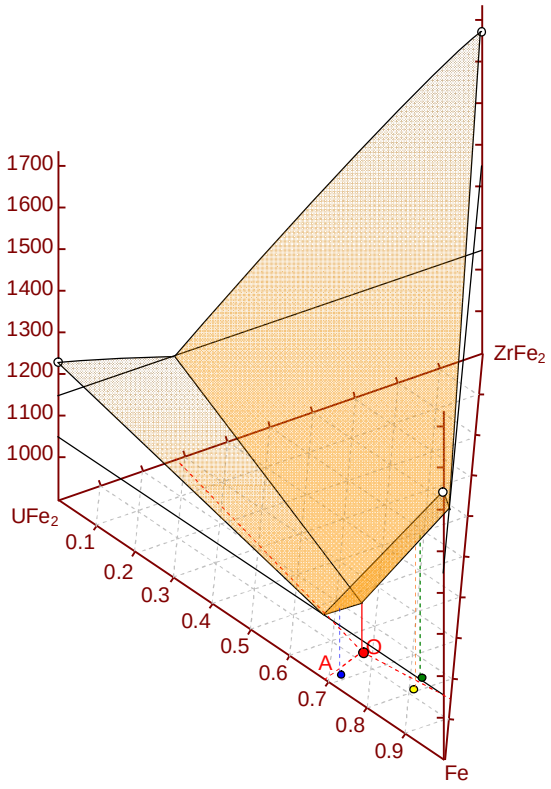

Fig. 3.6. Diagram of the $ZrFe_2$-UFe_2-Fe system

The obtained results are compared with the experimental data in Tab. 3.1.

Table 3.1

Comparison of experimental and calculated data

Ternary eutectic	U	Zr	Fe	T_{eut}
	mol. %			°C
Eut_{MC6}	13.39	1.19	85.42	1079
Eut_{MC7}	14.72	2.15	83.13	1096
Eut_{MC8}	13.03	3.33	83.64	1099
Calculated	12.5	7.7	79.8	1024

Comparison between the experimental and calculated data shows the obtained results to be in sufficient agreement. It should be stressed that the possible errors in calculations are due to the low reliability of initial data on the U-Fe phase diagram, and hence overestimation of zirconium content in the ternary eutectic in comparison with the values recorded in various tests of the METCOR Project. It should be noted that adjustment of the thermodynamic model, which may lead to convergence of experimental and calculated values of zirconium content in the eutectic point, will at the same time lead to a higher eutectic temperature, roughly up to 1040-1050°C.

On the other hand, the difference between the calculated and experimentally obtained eutectic compositions may be due to the crystallization path described below. After the most refractory component, i.e. Fe, has crystallized, the system finds itself at an A-O eutectic line, along which crystallization of the system proceeds until it reaches the ternary eutectic point. Since the identification of the eutectic crystallization along the eutectic line and at the ternary eutectic point by visual parameters is practically impossible, it may well be that this is just the situation with the experimentally observed eutectic patterns. Such a character of crystallization of the system is confirmed by great differences in zirconium content in the experimentally determined compositions.

Thus, the mechanism of interaction between the suboxidized corium and steel may be presented as follows:

Within approximately 20 min the temperature on the specimen upper top sets at ~1400°C. The temperature gradient in the crust C-66.2 (see Tab. 1.2.2) adjacent to the specimen top is from ~1400°C to ~2080°C (T_{sol} for C-70).

At the initial stage, uranium diffusion from the crust layer and, at first, formation of the UFe_2 compound at the crust – steel interface take place, followed by the eutectic melt formation at the contact of this compound with steel (see Fig. 3.3.). Then the interaction becomes the liquid phase process and enters a more rapid stage of development. Such non-oxidic components of the system, as steel components and the suboxidized corium components (U, Zr), dissolve in the originated melt. Composition of the forming melt depends on the relation between the rates of components transport to the melt and rates of their dissolution in the melt. Seemingly, the latter rates are not a limiting factor.

As it follows from experimental data, the originated melt is rich in iron, so it may be supposed that the process that determines the rate of melt formation at the steel – corium interface is the transfer of uranium into the interaction zone. The key role of uranium in melt formation is likely to have two reasons. Firstly, as the experimental data show, the rate of uranium intergranular diffusion is noticeably higher than that of zirconium. Besides, the eutectic temperature of UFe_2–Fe (1055°C) is significantly lower than that of $ZrFe_2$-Fe (1337°C), it being the factor determining the highest rates of interaction in the given system at relatively low temperatures in the area of 1055°C.

After formation of the melt of eutectic composition, the following processes seem to start:

1. Steel components dissolve in the eutectic melt.
2. Components of the formed metallic melt diffuse into corium along the grain boundaries and, as they advance, get enriched in non-metallic components of corium. It should be noted that with the advance of the non-oxidic to a higher temperature domain, it becomes enriched in zirconium to a considerable degree, especially at reaching temperature values close to or exceeding the temperature of the $ZrFe_2$-Fe eutectic (see Fig. 3.6).

Also noteworthy is the special character of interaction between components of the system, which is associated with its thermogradient condition. In this case, it may be possible to observe some effects caused not only by the concentration gradient, but also by the temperature gradient, for example, thermogradient diffusion.

Another process capable of significantly influencing the character of interaction between steel components and corium is the fluctuation of crystallization in the system stimulated by high values of heat flux.

Like in MC6 and MC7, advance of the metal – corium components interaction front stops at the isotherm that is slightly above the solidus, i.e. the eutectic of a multicomponent system composed of steel components and molten corium. Therefore, the interaction of steel with corium components slows down sharply at the transition from the liquid phase regime to the solid phase one.

It should be noted that the temperature overshoot above the eutectic temperature at the boundary of the zone of interaction with steel (after the interaction front has stopped its advance) is at its maximum in MC8, in contrast to MC7 when its was at its minimum.

Depending on the temperature at the boundary between the crust and specimen and, hence, position of the isotherm corresponding to the solidus, the interaction and equilibrium involve a definite amount of steel.

It should be noted that shortening of the incubation period in the test in question, if compared to MC6 and MC7, is most obviously connected with the increased volume fraction of the $U(Zr)O_2$-based solid solutions in the crust, which serve as active carriers of uranium to the interaction boundary and facilitate a more rapid accumulation of the eutectic liquid in the amount required for the fast stage.

Conclusions

In MC8, the ablation of vessel steel at its interaction with molten corium C-70 has been examined in argon during 12 hours, the maximum temperature of the steel specimen top being 1425°C. Dimensions of the degenerated steel area are close to those in MC6.

The performed investigations yielded the following results:

1. The advance rate of the boundary of degenerated steel area into the steel specimen body has been measured by means of ultrasonic echolocation. The incubation period of the degenerated area appearance was ~3 hours. The initial advance rate of the front of steel degeneration was estimated at 1.17 mm/h. In the end of the test the rate was 0.32 mm/h.
2. Metallographic studies of a specimen axial cut yielded profiles of the upper and lower boundaries of the interaction zone. The lower boundary is shown to coincide with the 1200 °C isotherm obtained by numeric calculation of the specimen temperature field. The maximum depth of the interaction zone equals 6.65 mm.
3. The disappearance of the acoustic defect and its traces has been registered. It evidences the complete meltdown of the degenerated steel zone.
4. The upper and lower zones of the corium ingot, the degenerated steel zone and steel of the initial specimen were subjected to SEM/EDX. Steel components were found only in the bottom part of the corium ingot. The degenerated steel structure is composed of dendrites and eutectic phase. The bulk composition of the degenerated steel (mass %) is: U - 21.3; Zr - 6.7; Fe - 67.9; the remainder are the alloying elements of steel. The dendrite crystals are composed of Fe - 92.4 mass %; the rest are the alloying elements of steel. The eutectic consists of (mass %) U - (32 - 37); Zr - (3.1 - 4.4); Fe - (56.5- 61.0); the remainder are the alloying elements of steel. The composition and structure of the non-degenerated steel have not changed. The crystallized crust layer was found to have a layered structure and contain large cubic monocrystals of the $U(Zr)Fe_2$ intermetallide compound at the ablation lower boundary.

References

1. Work Plan for METCOR, Phase 2 Project.
2. Khabensky V.B. et al. Measurements of vessel steel thermal conductivity. Progress Report.// NITI, METCOR, Phase 1.
3. V.B. Khabensky et al. Investigation of corium melt interaction with NPP reactor vessel steel (METCOR). Phase 2. First year. Annual technical report № 1-833.2-2003 (Append. 3)// NITI
4. N.F. Losev. Quantitative X-ray fluorescence analysis. M. Nauka Publishers, 1969, 366 p. (in Russ.)
5. D.I. Riabchikov, M.M. Seniavin. Analytical chemistry of uranium. M. Publishing House of the USSR Academy of Sciences. 1962. (in Russ.).
6. V.F. Lukyanov, S.B. Savvin, I.V. Nikolskaya. Photometric detection of uranium microquantities using reagent arsenazo III. JACh., V. XV, Issue 3. 1960. (in Russ.).
7. Fyodorov A. A. New methods of metallic powders and slags analysis // M.: Metallurgiya Publishers, 1972. (in Russ.).
8. Scoog D., West D. Fundamentals of Analytical Chemistry. Vol.1 & 2. Mir Publishers, 1979. (in Russ. translation).
9. Markov V. K. et al. Uranium. Methods of its determination // M.:, Atomizdat Publishers, 1964. (in Russ.).
10. GOST 4011-72. Drinking water. Methods for determination of total iron.
11. Sendel E. Methods of metal traces determination by colorimetry // M.: Mir Publishers, 1964 (in Russ.).
12. Harvey, Smart, Amis, Anal. Chem., 27, 26 (1955).
13. Khabensky, V.B. et al. Methods of physico-chemical analysis // Progress report. NITI, MC-02/99, July 1999, (in Russ.).
14. Butirin, G.M.. High-porosity carbon materials. M.: Chemistry, 1976,192 p. (in Russ.).
15. P. Gordon, A.R. Kaufmann // Trans. AIME, 1950, v.188, p.182-184.
16. G.G. Michaud // Canadian Met. Quart., 1966, v.5, No.4, p.355-365.
17. D. Arias, J.P. Abriata // Bull. Alloy Phase Diagr., 1988, v.9, No.5, p.597-632.